https://doi.org/10.5194/essd-2024-578
Preprint. Discussion started: 12 February 2025

A revised and expanded deep radiostratigraphy of the Greenland Ice Sheet from airborne radar sounding surveys between 1993–2019

Joseph A. MacGregor[1], Mark A. Fahnestock[2], John D. Paden[3], Jilu Li[3], Jeremy P. Harbeck[4], Andy Aschwanden[2]

[1] Cryospheric Sciences Laboratory, NASA Goddard Space Flight Center, Greenbelt, Maryland, United States of America
[2] Geophysical Institute, University of Alaska Fairbanks, Fairbanks, Alaska, United States of America
[3] Center for Remote Sensing and Integrated Systems, The University of Kansas, Lawrence, Kansas, United States of America
[4] ADNET Systems, Bethesda, Maryland, United States of America

Correspondence to: Joseph A. MacGregor (joseph.a.macgregor@nasa.gov)

Abstract. Between 1993 and 2019, NASA and NSF sponsored 26 separate airborne campaigns that surveyed the thickness and radiostratigraphy of the Greenland Ice Sheet using successive generations of coherent VHF radar sounders developed and operated by The University of Kansas. Most of the ice-sheet's internal VHF radiostratigraphy is composed of isochronal reflections that record its integrated response to past centennial-to-multi-millennial-scale climatic and dynamic events. We previously generated the first comprehensive dated radiostratigraphy of the Greenland Ice Sheet using the first 20 of these campaigns (1993–2013) and investigated its value for constraining the ice sheet's history and modern boundary conditions. Here we describe the second major version of this radiostratigraphic dataset using all 26 campaigns, which includes substantial improvements in survey coverage and was mostly acquired with higher-fidelity systems. We incorporated several lessons learned from our previous efforts for improved quality control and accelerated tracing, including an automatic test for stratigraphic conformability, a cutoff length for semi-automatic tracing propagation, a thickness-normalized reprojection for radargrams, and automatic inter-segment reflection matching. We reviewed and augmented the 1993–2013 radiostratigraphy and applied an existing independently developed method for predicting radiostratigraphy to the previously untraced campaigns (2014–2019) to accelerate their semi-automatic tracing. The result is a more robust radiostratigraphy of the ice sheet that can validate the sensitivity of ice-sheet models to past major climate changes and constrain long-term boundary conditions (e.g., accumulation rate). Based on these results, we make several recommendations for how radiostratigraphy may be traced more efficiently and reliably in the future. This dataset is freely available at https://doi.org/10.5281/zenodo.14531734 (MacGregor et al., 2024). It includes all traced reflections at the spatial resolution of the radargrams and grids (5 km horizontal resolution) of the depths of isochrones between 3–115 ka and ages between 10–80% of the ice thickness; associated codes are available at https://doi.org/10.5281/zenodo.14183061 (MacGregor, 2024a).

1 Introduction

The Greenland Ice Sheet (*GrIS*) is losing mass rapidly and is projected to do so for the foreseeable future unless substantial mitigation of anthropogenic warming is undertaken (Aschwanden et al., 2019; Goelzer et al., 2020; Otosaka et al., 2023). Ice-sheet models are the essential tools used to make these projections, but the uncertainty in these projections is large and significantly affects how society might respond to the global and regional sea-level change caused by GrIS wastage (Aschwanden et al., 2021). Numerous efforts are underway to reduce this uncertainty (e.g., Aschwanden and Brinkerhoff, 2022), and among the major challenges that these efforts seek to address are the initialization of these models prior to applying projected external forcings (typically atmospheric and oceanic) and whether their long-term sensitivity to anthropogenic climate change is consistent with that inferred from paleoclimatic records (e.g., Goelzer et al., 2018; Briner et al., 2020). Fortunately, the GrIS contains within itself a substantial and spatially well-distributed archive of its integrated response to past climate change: its isochronal radiostratigraphy. Further, this radiostratigraphy can constrain the subsurface state and dynamics of the present-day GrIS in a manner not achieved by other spatially-distributed observations; it is also potentially valuable for identifying well-initialized instances of ice-sheet models.

MacGregor et al. (2015a) (hereafter *M15*) generated the first large-scale dated radiostratigraphy of the GrIS. That study was made possible by the abundance of high-quality very high frequency (*VHF*) airborne-radar sounding data collected in the prior two decades (1993–2013, all years CE) sponsored by the United States' (*US*) National Aeronautics and Space Administration (*NASA*) and National Science Foundation (*NSF*; CReSIS, 2024), advances in radar-sounder design led by The University of Kansas (*KU*; e.g., Gogineni et al., 1998) and its Center for Remote Sensing and Integrated Systems (*CReSIS*; e.g.,; Rodríguez-Morales et al., 2014; Arnold et al., 2020), and a suite of synchronized deep ice cores collected by international consortiums led primarily by Denmark and the United States (e.g., Dahl-Jensen et al., 2013; Rasmussen et al., 2013; Seierstad et al., 2014; Mojtabavi et al., 2020). M15 introduced several advances in prediction, mapping, dating, validation and gridding of radiostratigraphy to generate the first ice-sheet-wide age volume for either of Earth's two remaining ice sheets. That study enabled numerous improvements in mapping of key ice-sheet boundary conditions (e.g., MacGregor et al., 2015b, 2016a,b, 2022; Dow et al., 2018). It also motivated refinements to – and assessment of – methods for mapping and modeling radiostratigraphy (e.g., Born, 2017; Xiong et al., 2018; Delf et al., 2020; Born and Robinson, 2021). However, no subsequent study has significantly improved upon the M15 dataset itself, either by infilling isochronal reflections that were unmapped by M15 or by incorporating the large quantity of additional similar airborne-radar sounding data collected as part of NASA's Operation IceBridge (*OIB*) in 2014–2019 that was not included in M15 (MacGregor et al., 2021).

Here we describe version 2 (*v2*) of the GrIS radiostratigraphy dataset and the methods to generate it, with a particular emphasis on methodological improvements introduced since M15 and remaining uncertainties. Based on the development of this dataset, we identify future opportunities for developing a more complete deep radiostratigraphy of the GrIS and make recommendations for future improvements in tracing methods.

2 Airborne radar-sounding data

To build this second version of the GrIS-wide radiostratigraphy, we first evaluate the same 1993–2013 VHF radar-sounding data collected over the GrIS by KU/CReSIS as M15 used to generate v1 (Table 1; Fig. 1; CReSIS, 2024). We further consider the additional six OIB campaigns worth of VHF radar-sounding data collected annually during boreal springtime between 2014–2019 by KU/CReSIS using identical or similar system configurations. These data were recorded coherently and subsequently focused using synthetic aperture radar (*SAR*) methods by KU/CReSIS. The nominal vertical resolution of these processed data is 2.5–4.4 m, which is sufficiently fine to resolve many (often dozens) distinct internal reflections, while their along-track resolution is more variable (~15–150 m depending on system and campaign). Depending on system performance, in-flight acquisition decisions and post-processing requirements, individual survey flights are composed of one or more *segments*, which can be tens to thousands of kilometers long depending on how many segments constitute each flight. Each segment is further divided into a sequence of ~50-km-long data *frames*, which are the format in which the data are distributed by KU/CReSIS. For example, the flight on 2011-05-02 (*20110502* in KU/CReSIS nomenclature), is divided into two segments, (20110502_*01* and 20110502_*02*, respectively), which are composed of 38 and 35 frames, respectively (20110502_01_*001*–20110502_01_*038*, and 20110502_02_*001*–20110502_02_*035*). We evaluate these SAR-focused data "as-is" and do not perform any substantive re-processing thereof, although we note that at least one focusing method has since been introduced that is intended to optimize detection of specular internal reflections (Castelletti et al., 2019).

Table 1: NASA/NSF/KU/CReSIS airborne radar sounding surveys of the GrIS between 1993–2019 considered in this study.

				Total length evaluated [d]		Length traced [e]				
Year	Aircraft type [a]	Radar sounder [b]	Priority rating [c]	v1 (M15) (km)	v2 (this study) (km)	v1 (km)	(%)	v2 (km)	(%)	v2–v1 change (km)
1993	P-3B	ICORDS	Low	17 205	1 703	4 243	25	868	51	–3 375
1995	P-3B	ICORDS	Low	13 641	4 053	6 640	49	3 853	95	–2 787
1996	P-3B	ICORDS	Low	4 527	249	2 999	66	249	100	–2 750
1997	P-3B	ICORDS	Medium	14 123	5 885	5 922	42	4 019	68	–1 903
1998	P-3B	ICORDS v2	Medium	25 977	7 052	11 538	44	3 993	57	–7 545
1999	P-3B	ICORDS v2	Medium	33 993	26 493	24 409	72	20 458	77	–3 951
2001	P-3B	ICORDS v2	Medium	10 899	4 530	2 623	24	2 880	64	+257
2002	P-3B	ICORDS v2	Medium	21 187	9 137	10 642	50	7 100	78	–3 542
2003	P-3B	ACORDS	Medium	13 988	7 950	6 022	43	4 865	61	–1 157
2005	DHC-6	ACORDS	Low	6 096	0	761	12	0	0	–761
2006	DHC-6	MCRDS	Low	12 289	268	1 796	15	122	46	–1 674
2007	P-3B	MCRDS	Medium	11 846	4 303	2 192	19	1 791	42	–401

2008	DHC-6	MCRDS	Low	22 706	8 802	7 438	33	6 526	74	–912
2009	DHC-6	MCRDS	Low	9 250	366	341	4	323	88	–18
2010	DC-8	MCoRDS	Medium	25 186	10 370	3 677	15	3 543	34	–111
2010	P-3B	MCoRDS	Medium	28 171	2 547	2 840	10	1 027	40	–1 813
2011	P-3B	MCoRDS v2	High	74 875	31 192	25 814	34	20 987	67	–5 727
2011	DHC-6	MCRDS	Low	7 172	708	660	9	328	46	–332
2012	P-3B	MCoRDS v2	High	88 278	34 791	23 192	26	22 270	64	–472
2013	P-3B	MCoRDS v3	Medium	41 494	11 663	16 484	40	7 011	60	–9 473
2014	P-3B	MCoRDS v3	High	(88 893)	35 460	N/A		26 374	74	+26 374
2015	C-130H	MCoRDS v5	Medium	(71 291)	450	N/A		346	77	+346
2016	WP-3D	MCoRDS v5	Medium	(27 134)	250	N/A		248	99	+248
2017	P-3B	MCoRDS v3	High	(78 841)	19 805	N/A		13 229	67	+13 229
2018	P-3B	MCoRDS v3	Medium	(42 189)	2 000	N/A		1 397	70	+1 397
2019	P-3B	MCoRDS v3	Medium	(59 419)	18 732	N/A		17 016	91	+17 016
			Total	482 902 (850 669)	248 758	160 233	N/A	170 823	N/A	+10 590

[a] See MacGregor et al. (2021) for additional detail on deployed aircraft.

[b] Radar sounder nomenclature follows KU/CReSIS nomenclature. They maintain a document that details system characteristics for all its surveys before 2010 (https://data.cresis.ku.edu/data/rds/rds_readme.pdf).

[c] The qualitative priority rating is described in §2.

[d] Total length evaluated includes all segments where the radar sounder was acquiring data, which sometimes includes segments that primarily overflew Arctic sea ice that is not relevant to this study. Gaps within segments are common in earlier campaigns (1993–2001) and complicate length calculations, so here we ignore gaps greater than 10 times the median distance between traces for each segment, leading to generally lower values for those earlier campaigns than reported by M15. Values in parentheses for v1 are campaigns that were not traced by M15. For this study (v2), the total length of the reduced set for each campaign is reported.

[e] Number of 1 km segments with at least one reflection traced (same metric as M15). Percentages are of the portion of the dataset evaluated, which differs between M15 and this study.

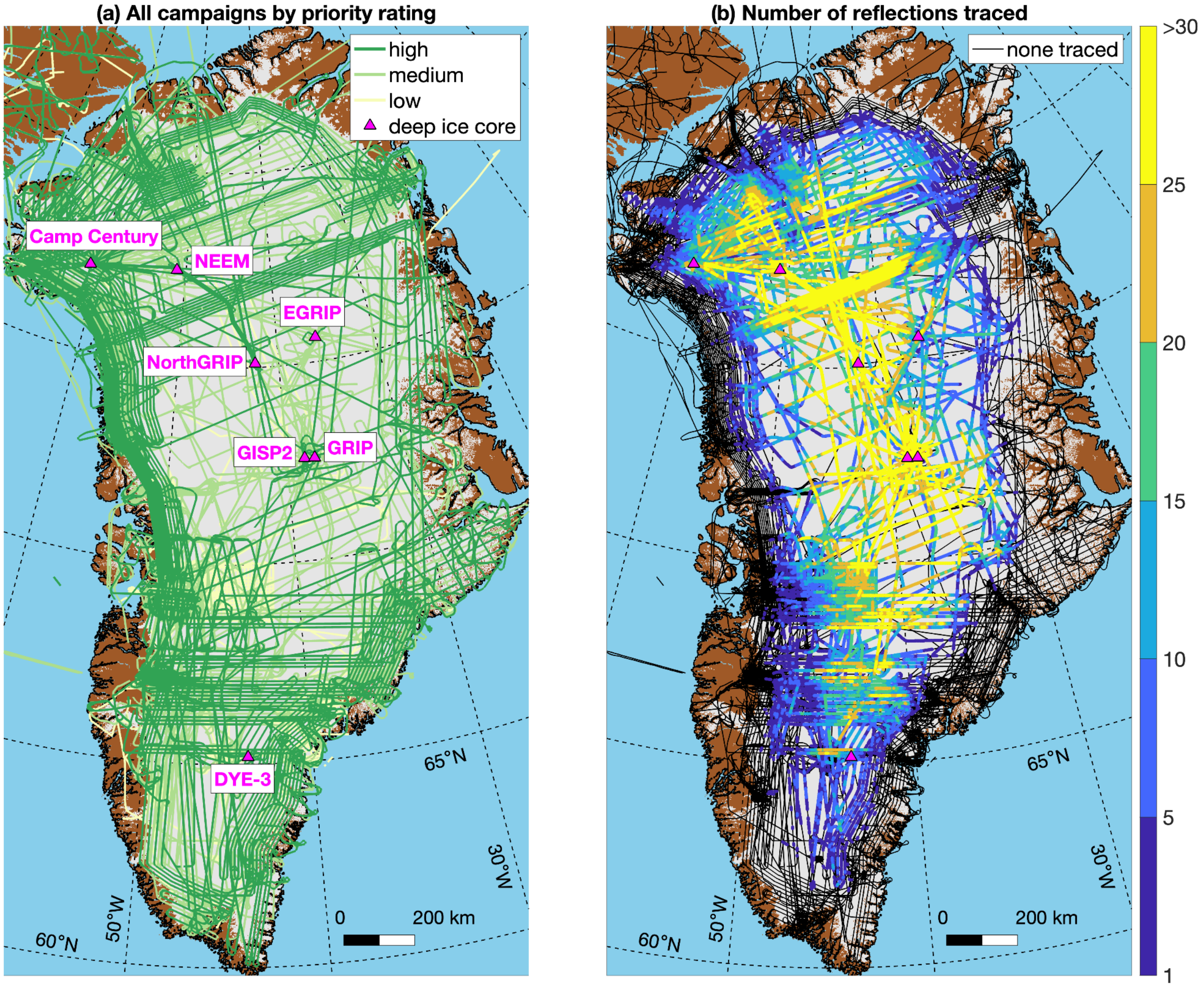

Figure 1: Airborne radar-sounding surveys collected across the GrIS by KU/CReSIS between 1993 and 2019. Segments are color-coded by (a) priority rating and (b) maximum number of reflections traced within 1 km segments along-track. Ice, land, and ocean masks are from Howat et al. (2014) via BedMachine v5 (Morlighem et al., 2022).

The two-way traveltimes of both the air–ice and ice–bed reflections have already been traced and recorded in these data by semi-automated algorithms and quality-controlled (*QC'd*) by KU/CReSIS personnel; the difference between these traveltimes has been used extensively by others to map ice thickness across Greenland (e.g., Morlighem et al., 2017, 2022). The ice–bed reflection is harder to trace confidently than the air–ice reflection, and during our examination of the dataset we occasionally observed possible errors in the former. However, because we are primarily interested in reflection depths, we only adjusted the air–ice reflection traveltime to address minor but obvious errors that we observed in a very small portion of the dataset that we evaluated (<0.1%). As for M15, when converting two-way traveltime t to depth, we assume that the radio-frequency real part of the relative permittivity of ice is 3.15, equivalent to a one-way radio-wave speed in ice of 168.9 m μs^{-1}.

A fundamental difference between M15 and this study revolves around the handling of "repeat-track" flights. This difference arises from the recognition that the lead priority for most NASA airborne surveys of the GrIS by OIB and its predecessors was detecting elevation change of the surface of the GrIS using laser altimetry along the same flight tracks repeatedly (e.g., Krabill et al., 2000; Csatho et al., 2014). In other words, many NASA flights that collected high-quality VHF radar-sounder data across the GrIS did so along a track that was nearly identical to another flight that did the same. M15 ignored this issue and evaluated all 1993–2013 data, which complicated subsequent reconciliation of traced reflections into an ice-sheet-wide radiostratigraphy due to, e.g., minor variations in flight track that lead to numerous intersections of two slightly different flights with each other. In this study, we explicitly avoid tracing repeat tracks by first collating what we term the *reduced set*. To collate this reduced set, we first assign each campaign a priority rating (Table 1), i.e., an *a priori* qualitative assessment of the campaign's overall radar data quality intended to guide prioritization for further tracing. This rating was mostly based on the radar system used and known campaign outcomes, but we recognize that individual intra-campaign segment quality can vary significantly due to several factors (e.g., environmental RF noise, data-acquisition interruptions, survey altitude change, GNSS or system-timing errors). We then manually inspected a map of the GrIS showing all radar flight tracks and identified all contiguous sets of frames required to "complete" a GrIS radiostratigraphy from the 1993–2019 KU/CReSIS data. If any portion of a track was repeated, then only a portion from the campaign with the highest available priority rating was included. While this approach means that many previously traced segments from v1 of the GrIS radiostratigraphy have been effectively discarded, it minimized the work required to review those data. As a result, M15 traced at least one reflection in ~33% of the dataset it examined, while this study more than doubled that ratio (69%; Table 1). Table 2 summarizes this step and all other major methodological differences between M15 and this study.

Table 2: Summary of key differences between the development of v1 (M15) and v2 (this study) GrIS radiostratigraphy datasets.

Element	v1 (M15)	v2 (this study)
Data selection	All frames from 1993–2013 were investigated.	Campaigns were initially prioritized (Table 1) and then the "reduced set" of non-overlapping frames from 1993–2019 was identified manually based on geolocation and visual assessment of segment quality. Only this reduced set was investigated.
Data pre-processing	Individual frames were reconstituted into ~50 km-long radargrams ("blocks") with ~1 km overlap on both ends for automated matching of reflections between them.	Individual frames were concatenated, regardless of length, and any pre-existing overlap between them (non-unique traces) was removed.
Reflection prediction	If complex radargrams were available, then phase-tracking was used; if not, then image processing (ARESP) was used, with the option for manual reflection prediction if both those methods failed.	Only ARESELP was used to predict reflections and only for previously untraced segments from 2014–2019.

Radargram visualization	Original (two-way traveltime), free-air-removed (“depth”) or reflection-flattened radargram views available.	Additional thickness-normalized view available where both ice–surface and ice–bed reflections were already traced.
Reflection selection	As many contiguous reflections as observed were selected to be traced.	Distinct and isolated reflections from the upper 80% of the ice column were prioritized for tracing, as these were assumed to be isochronal.
Reflection tracing	Semi-automatic peak following or manual tracing was used, with no cutoff length for the traced reflection.	Semi-automatic peak following was used, with an adjustable cutoff length (typically 10–100 km) to limit erroneous excursions and an automatic stop upon intersection with an existing traced reflection.
Reflection flattening	Either predicted or traced reflections could be used to flatten the radargram for QC and further tracing.	The flattening algorithm was adjusted to consider traced length (indicative of overall quality) rather than just the maximum number of traced reflections to identify the reference location, and it was improved to iteratively predict the depth of reflections not observed at the reference location (where they overlapped with other reflections that did).
Reflection tracing QC	Once all blocks for a given segment were traced, they were merged and displayed in a separate graphical user interface (*GUI*) for QC.	No additional merging was necessary; after any reflection was traced or adjusted, the GUI required that the sign of the depth difference between each reflection pair be the same throughout the radargram, i.e., that all reflections be stratigraphically conformable with respect to each other.
Reflection matching	Reflections were matched manually using a combination 2-D/3-D GUI, which were then QC’d using network graphs to check for reflection overlap.	Reflections were initially matched automatically based on their depths and the range resolution of the segment’s radar system; these matches were then manually QC’d and supplemented using a 2-D-only GUI.
Firn correction	None applied but a 10 m uncertainty in reflection depth was assumed.	For each trace, the modeled firn air content closest to the acquisition date was used to estimate the firn correction, and the assumed reflection depth uncertainty was reduced to 5 m.
Reflection dating	All six available deep ice cores were used to date reflections that intersected those cores; reflections that were matched to those core-intersecting reflections were dated, and the ages of remaining undated reflections were vertically interpolated where possible.	No major changes, except for the addition of EastGRIP ice core.
Reflection gridding	Normalized isochrone depths were gridded using ordinary kriging onto a 1 km grid.	Similar gridding method but using absolute isochrone depths and onto a 5 km grid, then smoothed.

To ensure the continuity of traced reflections within individual segments and reduce the computing resources required, M15 reconfigured individual radar data frames so that they partly overlapped with each other (typically by ~1 km). However, this process often created more challenges than it solved. In the intervening decade since that study, available computing resources have grown substantially but the data volume of any given SAR-processed segment from the radar systems deployed has remained the same. Here we simply concatenate contiguous sets of frames as needed for the reduced set, removing any non-unique traces that are present (whether in time or space). This procedure resulted in 536 sets of concatenated radar data frames that range between 12–3774 km long, with a median length of 250 km. We ultimately traced at least one reflection in 496 (93%) of those concatenated sets.

3 Reflection analysis methods

In this section, we describe the methods we used to trace GrIS radiostratigraphy, QC and date the dataset, focusing primarily on the key differences between this study and M15, all of which were made with the intent of accelerating product development and decreasing uncertainty therein. Table 2 summarizes those key differences in our methodology for pre-processing, predicting, tracing, QC'ing, dating and gridding GrIS radiostratigraphy. Fig. 2 shows the key elements of this workflow.

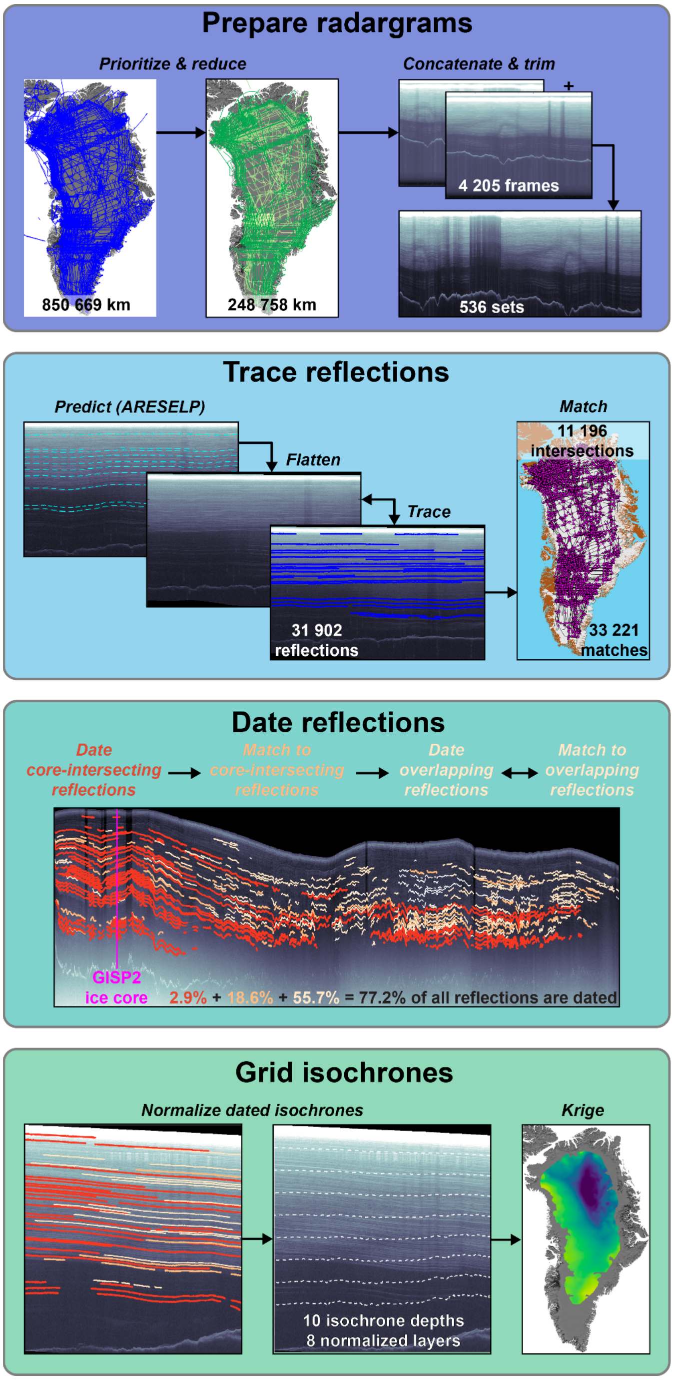

Figure 2: Flowchart illustrating the key steps involved in generating GrIS radiostratigraphy v2.

3.1 Tracing workflow

It is much simpler to confidently trace any reflection if a prediction of its location can be generated automatically beforehand. M15 introduced two automatic methods that leveraged the phase change of the recorded complex signal to predict the slope of internal reflections and – by integrating these slopes along-track – the shape of the reflections themselves. However, these methods were limited by the availability of large-volume, single-channel complex data from KU/CReSIS, and they cannot be applied to data that has already been SAR-focused. In cases where complex data were not available (i.e., most of the 1993–2013 dataset), Automated Radio Echo Sounding Processing (ARESP) was applied, using a refactored version of the ARESP algorithm introduced by Sime et al. (2011). However, all three methods focus on estimating reflection slope, as do similar methods introduced later (e.g., Holschuh et al., 2017). As a result, it is often difficult to determine where to automatically terminate a given reflection prediction in a manner comparable to that which often occurs with observed reflections, e.g., they fade out or merge with another reflection. This challenge tends to limit the use of slope-prediction methods to well-behaved radargrams with stable and relatively high signal-to-noise ratios.

Alternatively, Xiong et al. (2018) introduced an alternative method that they termed the Automated RES Englacial Layer-tracing Package (ARESELP). This method first identifies candidate reflection peaks vertically using wavelet transforms, prior to then propagating these candidate reflection peaks horizontally using Hough transforms for slope prediction. Because their method does not require complex data, permits reflections to terminate, often generates realistic synthetic radiostratigraphy and was publicly archived, we selected this method for reflection prediction in previously untraced campaigns (2014–2019). We refactored the ARESELP algorithm (written in MATLAB™) to both accelerate it and improve QC of its output; we then applied it to the 2014–2019 campaigns (Fig. 3a). Despite our improvements, ARESELP is only used to predict reflection geometry and not as a substitute for tracing itself, as its output quality is variable (Jebeli et al., 2023). For example, ARESELP often identifies the multiple of the air–ice reflection as a candidate internal reflection. Where ARESELP is successful, its outputs were used only to initially "flatten" the radar data (described below) and then discarded, so that no ARESELP-predicted reflections were mistaken for operator-traced ones.

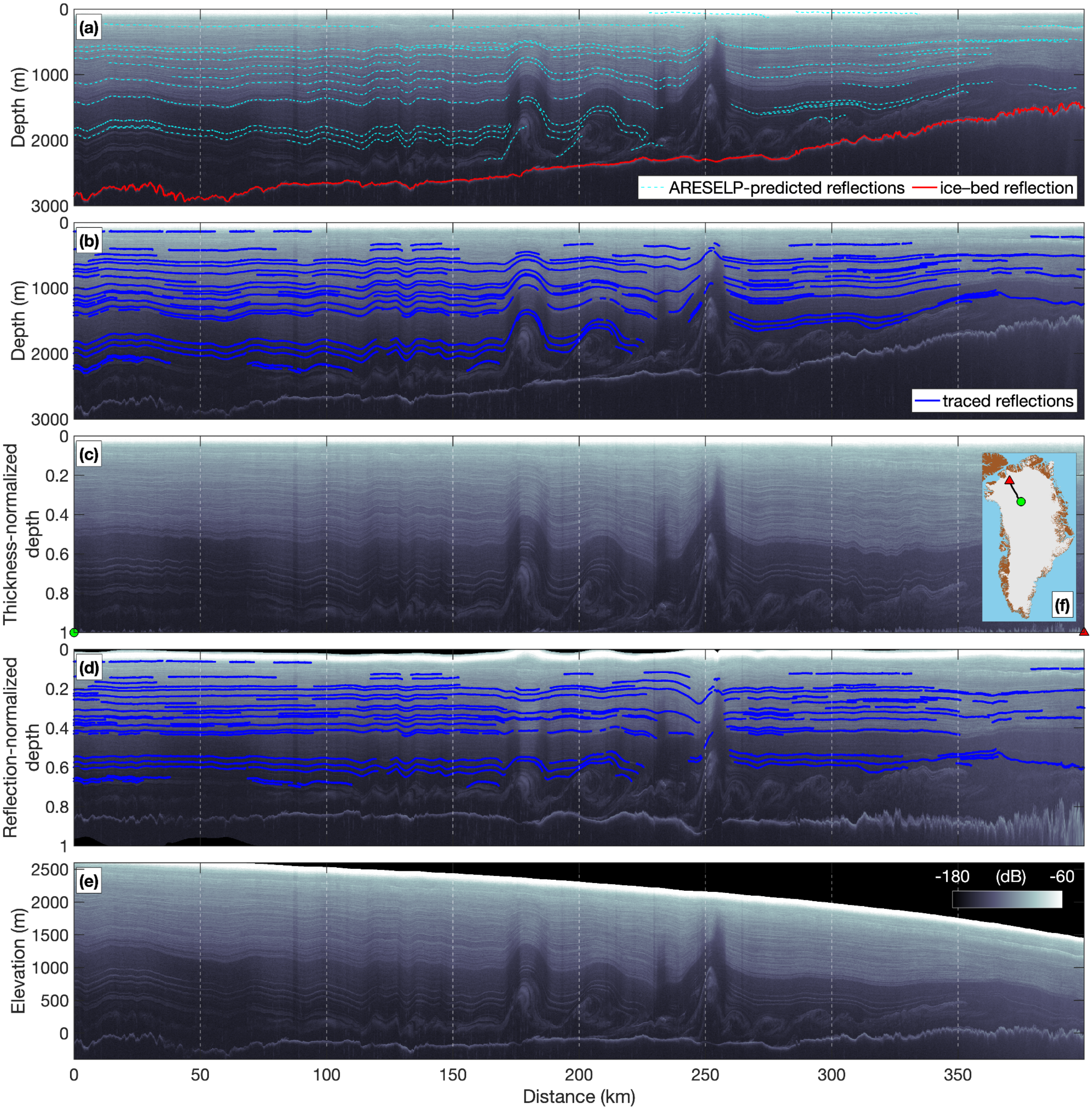

Figure 3: Multiple visualizations of a portion of a single segment (8 concatenated frames) from 2017-04-13 (20170413_01_049–056) that approximately follows ice flow from a central ice divide toward the outlet of Petermann Glacier. All radargrams shown at the same color scale. (a) Untraced radargram in terms of depth, i.e., the variable-length portion of the radargram before the air–ice reflection has been removed, with ARESELP-predicted reflections overlain. (b) Same as (a) but with traced reflections overlain. (c) Thickness-normalized radargram. (d) Reflection-flattened radargram. (e) Elevation-corrected radargram (relative to geoid). (f) Location of radargram in Greenland.

As illustrated by M15, flattening radar data with respect to predicted or already-traced reflections is both a valuable QC method and one which can accelerate further tracing (Fig. 3d). Here we continue to use this method with minor adjustments that permit it to more reliably and iteratively estimate the vertical position of reflections that were not observed at the reference location but which overlap with ones that were. However advantageous, this flattening method requires that either predicted or traced reflections are already available, which is not always the case. Inspired by earlier studies concerned with the physical interpretation of radiostratigraphy and modeling thereof, especially Nereson et al. (1998) and Hindmarsh et al. (2006), here we introduce an additional radargram reprojection that is *thickness-normalized*, which requires only that the air–ice and ice–bed reflections already be traced, as is the case for nearly all the KU/CReSIS dataset we evaluated. Normalization by ice thickness is commonly applied in analytic and numerical models of ice flow to ease interpretation, but to the best of our knowledge it has not been applied previously to the returned power P_r displayed in radargrams themselves, even though it can accelerate tracing. In the nomenclature of Hindmarsh et al. (2006), thickness normalization of radargrams also offers a rapid way of evaluating whether internal reflections drape over subglacial topography (i.e., they are essentially a shallower and smoother version of the ice–bed reflection) or override it (i.e., variations in reflection depth bear little resemblance to the ice–bed reflection and are mostly negligible). Following thickness normalization, draping reflections should be flatter, while overriding ones could be rougher. In practice, because relatively few of the flight tracks considered here both follow present ice flow *and* contain interpretable radiostratigraphy (Sime et al., 2014; Cooper et al., 2019), such a straightforward glaciological evaluation (draping vs. overriding) is often difficult. We note that alternative physically based vertical reprojections of radar data are conceivable, such as the coordinate transform for ice-flow models described by Parrenin et al. (2006), but here we focus on the simplest to implement and interpret for reflection tracing.

To perform this thickness normalization, the surface and bed traveltimes, $t_s(x)$ and $t_b(x)$, respectively, are first smoothed using a 3-km-long locally weighted filter in the along-track direction x. The normalized depth coordinate $\hat{z}$ is $(t - t_s(x))/(t_b(x) - t_s(x))$. Because $t_s(x)$ and $t_b(x)$ both vary along-track, the number of fast-time samples that form the radargram between them also varies, so the vertical interval between samples $\Delta\hat{z} = \hat{z}_{i+1} - \hat{z}_i$ also varies along-track. The thickness normalization is a vertical rescaling that does not directly alter the returned power $P(x,t)$ that constitutes the radargram, so if the vertical resolution of the displayed radargram can also vary along-track, then the thickness-normalized returned power $\hat{P}(x,\hat{z})$ can be displayed with no change in amplitude from $P(x,t)$. In practice, it is simpler and more computationally efficient to display two-dimensional (*2-D*) matrices with two monotonic axes. Thus, the second and final step is to vertically interpolate $P(x,t)$ onto a single monotonic $\hat{z}$ vector that has the same number of samples as the original radargram and ranges from 0 to 1, which sometimes slightly degrades the signal-to-noise ratio of $\hat{P}(x,\hat{z})$ relative to $P(x,t)$. As for reflection-based flattening, reflection traveltimes can be similarly vertically reprojected, or traced within this projection and then reprojected to the radargram's original vertical frame of reference (t). This reprojection is simpler than that for reflection-based flattening, is also parallelizable, and it is particularly valuable for initial reflection tracing within radargrams where $H(x)$ varies substantially, as it reduces the need to adjust the vertical axis when tracing.

In terms of selecting which reflections to trace, for v2 we focused exclusively on those that we deemed most likely to be isochronal. Specifically, we focused on distinct, relatively isolated reflections in the upper ~80% of the ice column that are observed across many radargrams, are not diffuse (i.e., difficult to trace using semi-automatic peak following), and do not form part of a disrupted basal unit. While the above criteria represent an effort to ensure the validity of a core assumption of our approach (reflection isochroneity), we are not aware of direct observations of unconformable reflections that are both within the GrIS interior and above disrupted basal units that contradict this assumption, as have been observed in Antarctica (e.g., Das et al., 2013). Deeper basal ice in the GrIS interior and strata exposed at the ice margin can clearly be disrupted, overturned and probably unconformable (Dahl-Jensen et al., 2013; MacGregor et al., 2015a, 2020; Panton and Karlsson, 2015; Bons et al., 2016; Leysinger-Vieli et al., 2018), so we mostly avoid tracing reflections within this zone unless they meet other criteria and are identifiable across a large distance or several radargrams. As a result, several deeper reflections mapped by M15, which were typically the top of disrupted basal units, were removed during our review of the v1 dataset.

We continue to use semi-automatic peak following to trace reflections, typically using a very narrow fast-time (vertical) sampling window (±1 sample; 1.7–5.3 ns, equivalent to 1.4–4.5 m, depending on campaign) between traces, but sometimes ±2 samples and rarely ±3 samples for especially steep reflections. The algorithmic speed of this method outweighs its relative simplicity, as it permits faster tracing *and* faster correction of inevitable errors therein. To limit these errors, we terminate propagation of a candidate reflection automatically once another existing reflection is intersected or where tracing has propagated a prescribed distance limit from the manually selected inception (typically 25–100 km, depending on radargram quality and reflection slope) – whichever is first.

A critical addition to the tracing workflow relative to M15 is an algorithmic check for stratigraphic conformability following the tracing of any reflection or modification thereof. This QC check simply requires that the sign (either >0 or <0) of the depth difference between any pair of reflections be both non-zero and the same throughout the radargram. In other words, no traced reflection can be both above and below another. This check automatically identified occasional tracing errors in the v1 radiostratigraphy that we rectified, and it simplified the process of QC'ing v2. Once tracing is complete, all reflections were vertically re-adjusted by $\leq \pm 1$ fast-time (vertical) sample to match the local maximum in P_r. This adjustment also increases the value of recorded reflection P_r values for future investigations (e.g., MacGregor et al., 2015b).

3.2 Inter-segment matching

Once tracing was complete, intersections between traced segments were identified automatically, with an algorithm that requires a minimum intersection angle of 5° between segments in map view and limits identified intersections to a maximum along-track density of 5 km within any given segment. The combination of the reduced set and these intersection selection criteria generated 24% fewer intersections than v1 (11 196 vs. 15 148), which simplifies subsequent reflection matching. Assuming a uniform reflection matching error rate, fewer matching errors will be made if there are fewer intersections to evaluate.

Matching reflections between traced segments and between distinct radar systems is a significant challenge for large radiostratigraphic datasets. While M15 evaluated automatic matching, they ultimately did not use it. Here we generate an initial set of reflection matches automatically, with an algorithm that limits inter-segment matches to those with a mean depth difference no more than three times the maximum range resolution of the segment pair's radar system (2.4–4.4 m for most systems considered) within 500 m of their intersection. These automatic matches were then QC'd using network graphs to verify stratigraphic conformability between reflection pairs, using an algorithm similar to that applied when tracing individual segments (§3.1), i.e., if a segment contains two reflection that overlap horizontally, then they cannot both be matched to the same reflection in another segment. Additional matches were then identified manually, which were then again QC'd using network graphs. In M15, matches were not permitted between the earliest campaigns (1993–1997) and later ones due to their difference in range resolution; here we permit such matches as prominent traced reflections were often similar across all campaigns.

3.3 Dating and gridding

Once traced, matched and merged, reflections must be dated to be of maximum value to the broader scientific community. Our dating algorithm is mostly unchanged from M15, to which we refer the reader for further details. We are unaware of any substantive improvement in reflection dating methodology developed since then, although alternatives exist if better estimates of accumulation histories or modern dielectric profiling ice-core data are available (Cavitte et al., 2021; Franke et al., in review). To date traced radar reflections across an ice sheet, multiple dated and synchronized ice cores are required. We use the same six deep ice-core depth–age scales as M15 (their Table 2), but supplement them here with the addition of the partially complete EastGRIP (*EGRIP*) depth–age scale from Mojtabavi et al. (2020). This depth–age scale includes the upper 1884 m of the ice column – approximately three quarters thereof given an ice thickness of ~2550 m – which records the period 0–15 ka. Compared to M15, we slightly relax the search radius within which a radar segment is considered to have "intersected" an ice core from 3 to 5 km, increasing the number of core intersections from 53 to 65. The use of the reduced set also decreases dependence on the Camp Century ice core, which was overrepresented in the v1 dataset (47% of all intersections, as compared to 31% in this study). We continue to use the "quasi-Nye" dating method introduced by M15 to vertically interpolate the age of undated reflections that are either sandwiched between or are near pairs of dated reflections. This method seeks the best-fit vertical strain rate that can match the depth–age relationship of the two bounding reflections, and then uses this vertical strain to interpolate the age of the undated reflection – or extrapolate where appropriate.

Previously, an undated reflection could only be dated if it did not cause the vertical profile of age anywhere in the segment to decrease with depth. Here we relax this requirement slightly to accommodate potential matches of vertically closely spaced reflections by instead requiring that the age of the putative dated reflection be within 5% of the uncertainty in age of adjacent dated reflections. This relaxation accommodates slight mismatches in age between reflections that intersect different ice cores. Finally, where sufficient dated reflections exist, we use quasi-Nye interpolation to estimate the along-track depth of a set of "synthetic" isochrones at predetermined ages. We include the same set of five ages generated by M15 (9, 11.7, 29, 57 and 115 ka) along with five more of additional paleoclimatic interest (3, 8, 12.8, 14.7, and 19 ka).

Similar to M15, we use ordinary kriging to grid the depths of the 1-D along-track isochrones onto a 2-D grid using the Python geostatistical simulation software package GStatSim (v1.0.6; MacKie et al., 2023). We also use quasi-Nye interpolation (M15) to infer the age at predetermined thickness-normalized depth intervals along all traced segments and then grid these ages as well. We select a 5 km grid in the standard EPSG:3413 projection – rather than 1 km as in M15 – to focus on the large-scale age structure of the ice sheet. Contrary to M15, we find that absolute depths are smoother at large scale than thickness-normalized depths, so we grid the former instead. We find that a zero-nugget spherical semivariogram model is a better representation of the experimental semivariogram of shallower/younger isochrones (≤19 ka), while an exponential model is better suited to deeper/older ones. For the age at regular depth intervals, we restrict the gridding to the middle 70% of the ice column (10–80% ice thickness) at 10% intervals as this depth range captures the range of most traced reflections (Fig. 4); we find that spherical variograms are most suitable at all depths. This normalized depth range is more conservative than for M15 (4–100% ice thickness at 4% intervals). Independent variogram models are applied to each depth/age, as opposed to a single variogram model as in M15. We apply a 2-D Gaussian smoothing filter to all the resulting grids to reduce noise from individual traced segments and fill in small, enclosed gaps using natural neighbor interpolation. Finally, we blank out any portions of the grid that would result in age overturning (unconformities) relative to other adjacent grids.

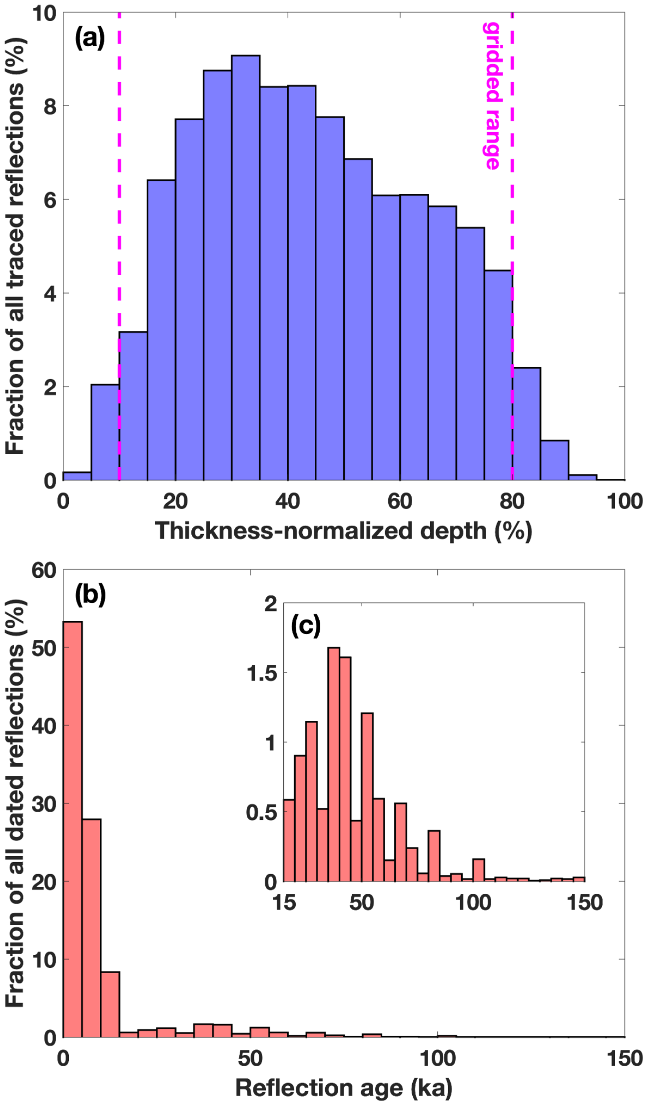

Figure 4: (a) Histogram of the normalized depth of all traced reflections (both dated and undated). Vertical magenta dashed lines highlight the normalized depth range for which the age of the ice sheet is gridded. (b) Histogram of the age of dated reflections. (c) Zoom-in of panel b on the pre-Holocene age range.

3.4 Depth and age uncertainty estimation

The depth uncertainty of the traced reflections is principally attributable to the assumed radio-wave velocity in pure ice and a correction for spatiotemporally variability firn air content. As for M15, we assume that the real part of the radio-frequency complex relative permittivity of pure ice ϵ'_{ice} is 3.15, equivalent to a radio-wave velocity in ice v_{ice} of 168.9 m μs^{-1}. M15 did not directly apply a firn correction and instead attributed a constant and uniform 10 m depth uncertainty to all traced reflections. Since then, substantial progress has been made in the modeling and validation of the firn air content in the near-surface of ice sheets, due to its importance for interpretation of satellite altimetry data (e.g., Medley et al., 2022). The total firn air content is equivalent to the firn correction that is commonly applied to radar-sounding data to correct reflection depths. Here we use the modeled firn air content developed by Medley et al. (2022) for the period 1980–2021 across Greenland and Antarctica to determine the local firn correction for each radar trace from the nearest 5-d simulation interval to the acquisition date. We then assume that the reflection depth uncertainty associated with the firn correction is reduced to 5 m. The median modeled firn correction applied is ~19 m, but it can be up to ~25 m.

The age uncertainty for each dated reflection is calculated following the same methods described in further detail by M15. For core-dated reflections, this total age uncertainty is the combination of the reported uncertainties in the ice-core depth–age scales (unchanged from M15), the depth uncertainty of the reflection (discussed above), and the uncertainty induced by the range resolution of the radar system used. The latter quantity depends on the signal-to-noise ratio (*SNR*) of the reflection at its closest approach to the ice core, which is typically ~5 dB, so for simplicity we assume that quantity is uniform for all core-dated reflections. For reflections dated using quasi-Nye dating, an additional uncertainty is included that accounts for the interpolation/extrapolation of age.

To estimate the uncertainty of the 2-D grids, we first also vertically interpolate the along-track depth (age) uncertainty of dated reflections to the age (depth) of interest and then krige these quantities using the same variogram model parameters as for their respective age (depth) of interest. These kriging-derived uncertainties are then combined with the kriged uncertainty for the parameter of interest (depth or age) as the square root of the sum of squares (M15 only considered the latter term).

4 Results

This second version of a radiostratigraphic dataset of the GrIS from NASA/NSF airborne radar-sounding data contains 31 902 individual traced reflections of widely varying lengths. Of these reflections, 2.9% were dated “directly” where they intersected ice cores, 18.6% by automatically or manually identified matches to those core-dated reflections, and another 55.7% using quasi-Nye dating, leaving 22.8% of traced reflections undated. Direct core-dating of reflections is essential but – following our particular tracing strategy – results in a very limited spatial distribution of dated reflections, mostly following the northern part of the central ice divide (Fig. 5). Reflections matched to those core-dated reflections significantly expand the coverage of dated reflections, especially in central and northern Greenland. Farther south, where reflections become discontinuous, age interpolation of dated reflections is especially important between ~65–71ºN. Undated reflections remain mostly around the periphery of the GrIS, in fast-flowing regions such as Sermeq Kujalleq, and in southern Greenland south of ~68ºN.

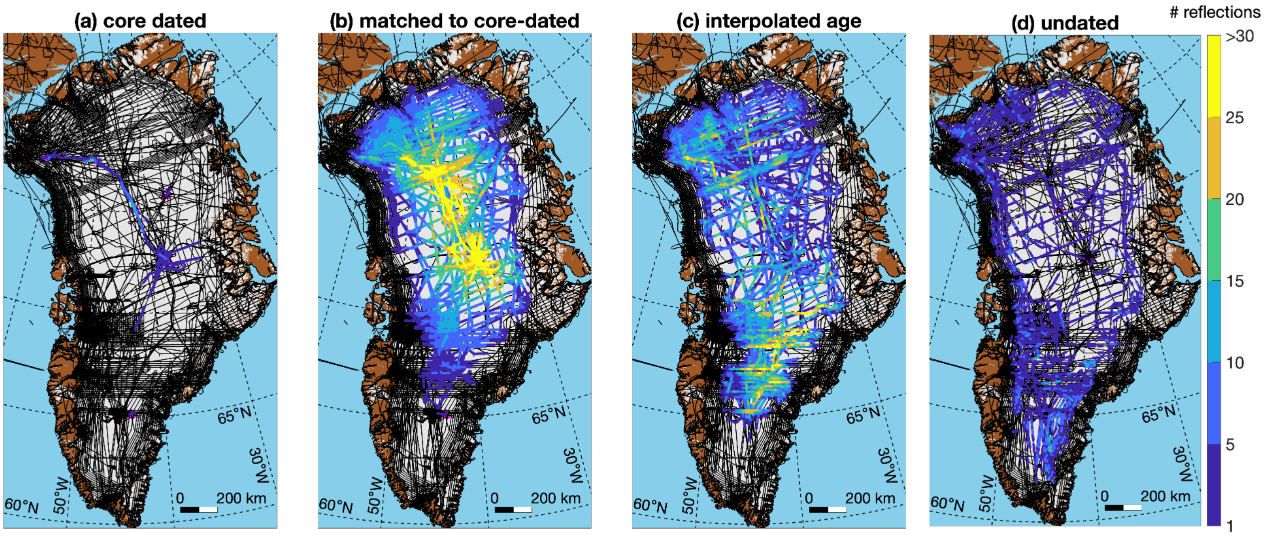

Figure 5: Number of traced reflections by the method in which they were dated.

For completeness and validation, we generated Movie S1, which shows all traced segments in an elevation-corrected reference frame. This movie illustrates both the breadth of the traced reflections and the considerable number of *un*traced reflections, which are typically discontinuous and less distinct – but not exclusively so. Most (94%) reflections were traced in a depth range within 10–80% of the ice thickness, following both our stated prioritization, signal loss with increasing depth, and the challenge of tracing distinct very shallow reflections within most of the KU/CReSIS dataset that we evaluated. The large majority (86%) of all dated reflections are from the Holocene (0–11.7 ka; Fig. 3b), which is consistent with previously observed patterns of radar reflectivity across the ice sheet. Some of the most distinct reflections are from the Last Glacial Period (11.7–115 ka), in particular the well-known trio observed throughout northern Greenland (37.7, 44.7 and 50.7 ka, respectively), so they are also often some of the most contiguous or readily matched between segments so they tend to be under-represented in the distribution of all dated reflections compared to numerous and sometimes difficult-to-match shallower Holocene reflections.

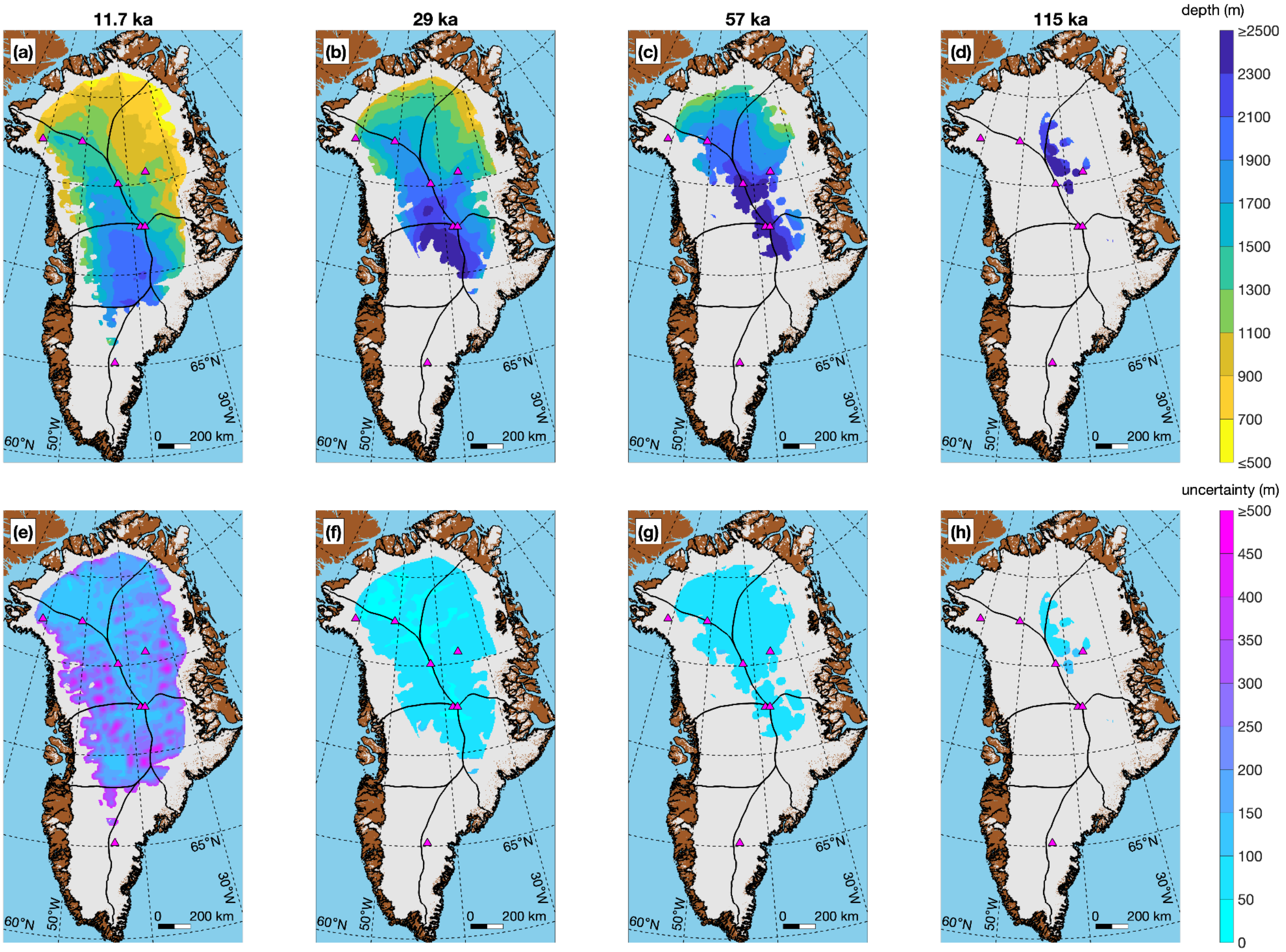

Figure 6: (a–d) Gridded depth of four out of the ten gridded synthetic isochrones (11.7, 29, 57 and 115 ka, respectively). (e–h) Gridded uncertainty in these isochrones. Ice drainage basins (black lines) are from Mouginot et al. (2019).

The resulting depth/age grids cover up to 65% of the ice sheet by area (Figs. 6 and 7). The uncertainties in the resulting datasets also are slightly more completely expressed than by M15. In comparison to similar depth/age grids produced by M15, it is clear that producing a dated GrIS radiostratigraphy within ~100 km of the ice margin or south of ~68ºN remains challenging. Neither version of the dataset does so consistently, except for v1 along parts of the northern margin of the GrIS, which we attribute to less conservative kriging parameters than those applied in this study. We attribute this broader challenge not to the sparsity of surveys (Fig. 1) but rather to the absence of traceable radiostratigraphy (less common) or the low continuity of observed radiostratigraphy (more common), which makes it less feasible to trace efficiently using this study's methods and was not prioritized (Movie S1). This result is consistent with earlier automated assessments of radiostratigraphic continuity by Sime et al. (2014) and M15, particularly in terms of where traceable radiostratigraphy is present (although not necessarily dateable).

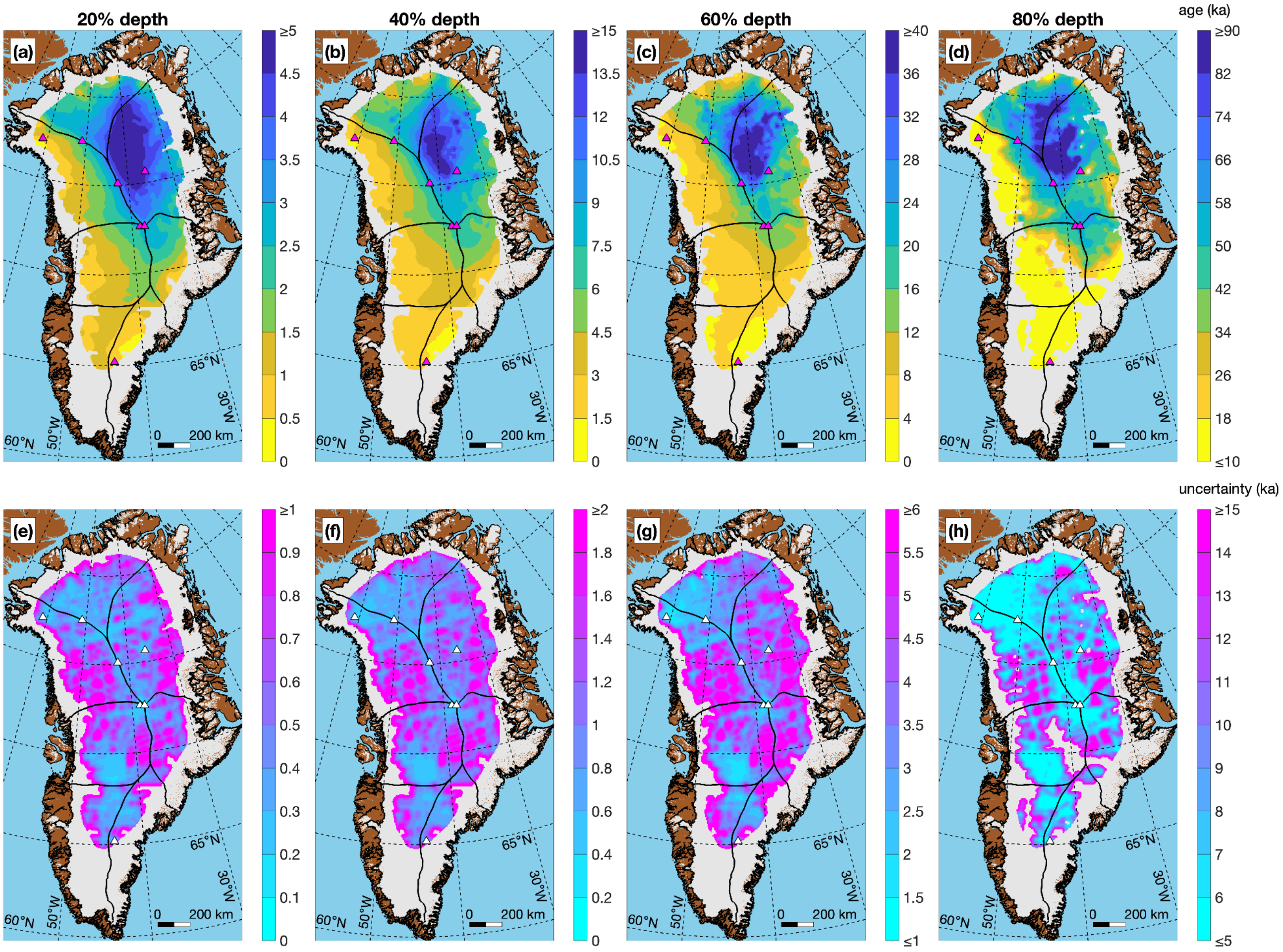

Figure 7: (a–d) Gridded age of four out of the seven gridded ages at 20, 40, 60 and 80% of ice thickness, respectively. (e–h) Gridded uncertainty in these ages. Note each panel has a different color scale, whereas for each row of Fig. 6 the color scale is the same.

As observed by M15 and reproduced here, the oldest ice at most depths is observed in the southeastern portion of the northernmost ice drainage basin and the northwestern portion of the northeastern drainage basin (northwest of the Northeast Greenland Ice Stream). Any potentially conformable Eemian ice (115–130 ka) is likely also located there (Fig. 6d). These results are qualitatively consistent with observations of outcropping pre-Holocene along the northern margin of the GrIS (MacGregor et al., 2020). Any substantial (>100 m) conformable layer of pre-Holocene basal ice is likely absent south of ~65ºN, which is consistent with the higher long-term accumulation rates there (e.g., MacGregor et al., 2016a).

The gridded uncertainty of the synthetic isochrones (Fig. 6e-h) varies significantly and does not necessarily increase with depth. Assuming comparable relative uncertainties for all dated reflections, it also depends on proximity (in age) of the synthetic isochrone to dated reflections. While reflections were regularly traced near the onsets and terminations of the Bølling-Allerød period (14.7–12.8 ka), the Younger Dryas cold period (12.8–11.7 ka) and the Holocene epoch (11.7 ka–present), much more common are yet younger reflections (Fig. 4a) from which the depth of those onsets/terminations were sometimes

https://doi.org/10.5194/essd-2024-578
Preprint. Discussion started: 12 February 2025

estimated. In contrast, the prominent trio of older reflections mentioned above that are often observed together in the northern GrIS represent a more spatially limited but stronger constraint on the location of some older climate transitions (e.g., Fig. 4f,g).

This study's gridded fields are generally similar to those in M15 (Fig. 8). We attribute most differences to improved coverage and QC in this study, the more conservative coarser grid resolution (5 km vs. 1 km) and the final smoothing applied. For the isochrone depths, as expected the differences increase toward the ice margin and away from ice core sites with a slight trend toward increasing magnitude with increasing isochrone age. The gridded age differences display a more complex spatial pattern. Their differences are lower at shallower depths, as expected, but increase significantly at 60% depth particularly in the older northern and northeastern drainage basins. At 80% depth – the maximum normalized depth we considered – the magnitude of the differences is large but varies in sign, with an increasing magnitude trend toward the north.

Franke et al. (2023) presented multiple gridded isochronal datasets for the northern GrIS from OIB and other campaigns led by the Alfred Wegener Institute (*AWI*), which could be compared to our gridded products. However, because they gridded directly traced isochrones, rather than the synthetic isochrones at climate transitions that we focused on, based on the ages of their isochrones alone most of our gridded isochrones are not directly comparable with theirs. Only one is potentially comparable with our 11.7 ka isochrone (Fig. 8a), which is their 12.0 ka isochrone for the Petermann Glacier onset region. However, given the two-order-of-magnitude difference in grid resolution between their isochrone (0.05 km) and ours (5 km), along with the smoothing we applied, we do not consider such a comparison meaningful.

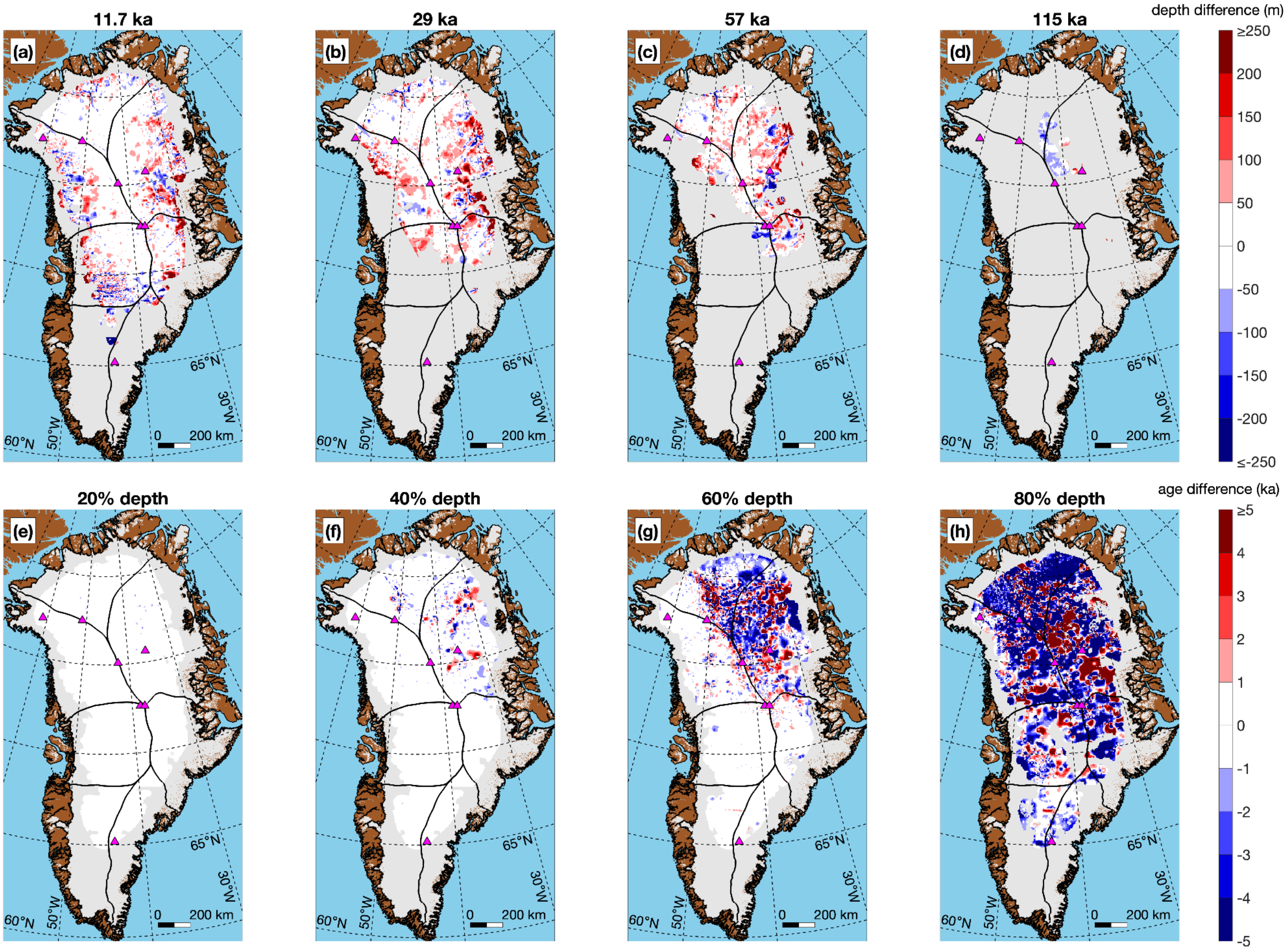

Figure 8: (a–d) Difference in gridded depth of four isochrones mapped by this study from M15. (e–h) Same as above, except for the age at normalized depths.

5 Discussion

Much has been written about the potential value of – and the challenge of producing – large-scale ice-sheet radiostratigraphy datasets (e.g., Karlsson et al., 2013; Sime et al., 2014; Moqadam and Eisen, in review; Bingham et al., in review). As with all methods of observation or data analysis, future improvements therein are almost inevitable. However, at some point the unique capabilities of the system in question – whether they be resolution, speed, accuracy or some other characteristic – must be locked so that the observation or analysis of interest can be made. Both M15 and this study assessed several methods for accelerating tracing but – critically – eventually paused that assessment and shifted gears to the actual production of an ice-sheet radiostratigraphy. This production stage revealed several challenges associated with QC'ing, dating and normalizing a large-scale radiostratigraphy (e.g., Fig. 2; §3), but several subsequent related studies have focused mostly on designing or assessing alternative methods for tracing or slope estimation (e.g., Panton, 2014; Delf et al., 2020), with relatively few that consider dating reflections not observed at ice cores (Cavitte et al., 2021). Further, it is now well established that it is relatively easy to trace many reflections in any one of the two dozen or so high-quality KU/CReSIS VHF radargrams that cross the northern GrIS (Fig. 1b; e.g., Panton, 2004; Xiong et al., 2018). It is much harder to trace discontinuous reflections within ~300 km of the ice margin, harder still within ~100 km, and even harder to confidently propagate ages from interior ice cores toward the periphery.

Despite the clear advantage of scale provided by our approach to mapping radiostratigraphy, our current approach possesses some limitations that could be addressed in future versions. A primary limitation is that – while the GrIS radiostratigraphy v2 dataset depends critically on the spatial relationships between segments and the matches between their traced reflections – it is not a modern relational database through which updates to any individual element propagate automatically. Instead, it is a series of static datasets developed in sequence (concatenated radargram segments, traced reflections, inter-segment reflection matches, reflection ages, and gridded depths/ages). In other words, if an error in tracing any reflection is identified and adjusted, then any matches between that reflection and others must be manually re-verified and the dating and gridding procedures would need to be re-run. A second but more tractable challenge is the dynamic display of intersecting segments and associated traced reflections on 2-D radargrams, which would clarify how far to attempt to trace reflections to maximize the potential for matching them between segments. Alternatively, such inter-segment relationships can sometimes be obvious in three-dimensional (*3-D*) perspectives of intersecting radargrams and their traced reflections (e.g., Franke et al., 2023). However, we experimented extensively with such 3-D perspectives in both MATLAB™ and PyVista (Sullivan et al., 2019) and found that modifying or matching mapped radiostratigraphy remains cumbersome in 3-D when evaluating many segment intersections (11 196 in this study).

To address the challenge of extracting useful geophysical information from large data volumes, machine learning (*ML*) methods have been increasingly deployed in many fields of Earth science. The constellation of ML methods clearly possesses great potential for accelerating the tracing of radiostratigraphy, but they face several broad challenges before they can be widely adopted (Moqadam and Eisen, in review; Moqadam et al., in review; Peng et al., 2024). First, most ML methods use supervised learning, which typically requires large training datasets. In this case, such datasets would be radargrams that have been traced exhaustively, i.e., those that possess few or no false negatives. However, all presently available large-scale radiostratigraphy datasets – including the one presented in this study – left innumerable observed reflections untraced. These reflections were typically less distinct, less bright or shorter – and so they were deprioritized in our workflow (§3.1). We suggest that suitable ML methods for tracing radiostratigraphy are those that can better tolerate inevitable and copious false negatives, perhaps by being trained on synthetic radargrams or using ARESELP-generated predictions (Culberg and Schroeder, 2021; Jebeli et al., 2023). A second and related issue is the question of which reflections should be traced. An answer with a future ML application in mind could simply be “all of them”, but perhaps a more realistic and readily achievable answer is “those that models seek to match”. In the latter more restrained scenario, which was implicit in our tracing strategy, we may consider both which observed reflections are clearly distinct from others *and* those which models seek to reproduce to better resolve GrIS history, i.e., typically those associated with or close to major climate transitions (e.g., Born and Robinson, 2021). However, how to enable ML to perform a similar prioritization remains unclear. Third, as emphasized by Delf et al. (2020) and applicable to all automated methods for tracing radiostratigraphy, improving our ability to automate the matching of reflections across discontinuities – whether due to an acquisition malfunction or observation limitation such as steep reflection slopes – remains an outstanding challenge, and it is not yet clear how ML can accelerate this process.

As originally conceived, this dataset (GrIS radiostratigraphy v2) would have included additional VHF airborne radar-sounding data collected primarily by institutions besides the US (Fig. 9). These include the first such data collected across the GrIS during the 1970's by a Danish–British–American consortium that was recently digitized by Karlsson et al. (2024), surveys of the northern and central GrIS mostly from the 1990s led by AWI (e.g., Nixdorf and Göktas, 2001), and more recent AWI surveys using newer CReSIS-built radar systems (e.g., Kjær et al., 2018; Franke et al., 2023). Including these data was ultimately beyond the scope of this study but remains possible and could help fill remaining gaps in coverage – especially in the northern half of the GrIS. A potential challenge in incorporating these data would be their different center frequencies and bandwidths, which result in different patterns of interfering reflections – particularly in reflection-rich Holocene ice. For the newer AWI data (2016–present), this challenge is due to the higher center frequency and wider bandwidth of the system used that would typically result in more reflections being distinguishable, whereas for the other mostly older data the challenge is reversed. Because we found that certain distinct reflections could be matched between KU/CReSIS systems from 1993 all the way through to 2019, there is reason for cautious optimism in merging such disparate datasets. Further, there is precedent in Antarctica for similar multi-system reconciliation of radiostratigraphy (Winter et al., 2017; Cavitte et al., 2021; Franke et al., in review).

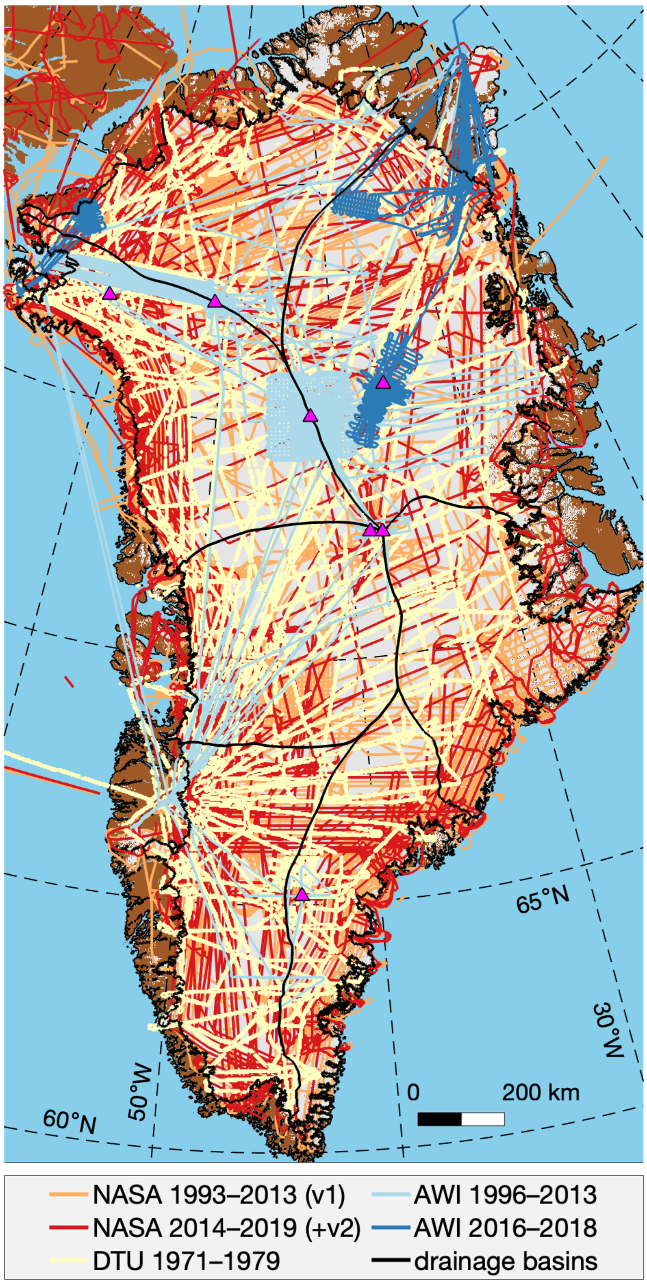

Figure 9: Airborne radar-sounding surveys collected across the GrIS led by various institutions that could be included in future versions of a GrIS radiostratigraphy (AWI: Franke et al., 2023; O. Eisen and D. Steinhage, pers. comm., 2020; DTU: Karlsson et al., 2024), as compared to that collected primarily by NASA/KU/CReSIS between 1993–2019.

Given its improved spatial coverage, more robust QC and more accessible data formatting (§6), we expect that this second version of the GrIS-wide radiostratigraphy will help fully realize part of the original purpose for generation of the M15 dataset – to "[provide] a new constraint on the dynamics and history of the [GrIS]" – but also to expand the range of potential applications for such a dataset. The v2 gridded products can be used to evaluate the modern age structure of initialized ice-sheet models to validate their overall climate sensitivity and various model parameterizations, especially past accumulation rates (e.g., Born and Robinson, 2021; Rieckh et al., 2024). Following the methods introduced by those recent studies, the capability to record and advect ice age non-diffusively using a Lagrangian approximation was also introduced recently (in v2.1) to the widely used Parallel Ice Sheet Model (https://www.pism.io/; e.g., Aschwanden et al., 2019), which expands the potential user base for model evaluation of the age structure of the GrIS. At coarser scales, the gridded datasets can be more reliably used to distinguish between Holocene and pre-Holocene ice, which is valuable for radiometric studies of radargrams (e.g., MacGregor et al., 2015b; Chu et al., 2018) and interpretation of bulk rheology (e.g., MacGregor et al., 2016a). Finally, the along-track traced reflections can be used to rapidly identify anomalous structures within the ice sheet that can be either diagnosed simply using steady-state models (e.g., MacGregor et al., 2016b) or targeted for more detailed diagnosis using structural analyses (e.g., Franke et al., 2022).

6 Code and data availability

The MATLAB™ GUIs, functions and scripts and Jupyter notebooks used to perform the analysis and generate the figures in this manuscript are available at https://doi.org/10.5281/zenodo.14183061 (MacGregor, 2024a). Most of the analysis was performed using functions built-in to several versions of MATLAB™ (R2022a to R2024b) with its associated Image Processing, Mapping, Statistics and Wavelet toolboxes. Python v3.12, various standard packages, and GStatSim were used to krige the dataset (MacKie et al., 2023).

The datasets resulting from this study, which together constitute version 2 of Greenland's deep radiostratigraphy, are available at https://doi.org/10.5281/zenodo.14531734 (MacGregor et al., 2024) and may also be later made available through the National Snow and Ice Data Center, where further dataset-specific documentation will be provided. Table 3 describes the format of the HDF-5-compatible MATLAB™ (.mat) files that contain each campaign's traced reflections for each segment. Table 4 describes the format of the GeoPackage (.gpkg) files that contain the depths of each segment's traced reflections, as we anticipate that these will be the most widely used reflection properties. These GeoPackage files are a more openly accessible version of the MATLAB files, but include many fewer reflection properties due to limitations of the format. Reflection ages and age uncertainties are preserved in each GeoPackage file's metadata. Table 5 describes the format of the NetCDF (.nc) file that contains the gridded (5 km horizontal resolution) isochrone depths and ages at normalized depths (§3.3, 4). For brevity, in these three tables, we describe only the key variables and not all preserved metadata or other attributes.

Table 3: Format of the "segment" structure in the MATLAB file for each campaign that contains the traced reflections at the radargram resolution.

Variable	Description	Units

name	Name of segment, including concatenated frames used	N/A
dist	Along-track distance, calculated using great circles and the WGS84 ellipsoid	m
lat	Latitude	°
lon	Longitude	°
num_layer	Number of traced reflections	N/A
num_trace	Number of traces in the concatenated segment	N/A
thick	Ice thickness	m
time	GPS measurement time since 0000-01-01	s
x	Projected x-coordinate, EPSG:3413	m
y	Projected y-coordinate, EPSG:3413	m
firn_corr	Modeled firn correction	m
stratigraphy	Structure with number of objects equal to num_layer that includes fields for each reflection property	N/A
stratigraphy.age	Reflection age	ka
stratigraphy.age_uncert	Uncertainty in reflection age	ka
stratigraphy.depth	Depth below ice surface to reflection (not corrected for firn)	m
stratigraphy.elev	Reflection elevation relative to WGS84 ellipsoid	m
stratigraphy.int	Reflection relative echo intensity	dB
stratigraphy.twtt	Englacial traveltime to reflection	s

Table 4: Format of GeoPackage files for each concatenated segment that contains the traced reflections at the radargram resolution.

Variable	Description	Units
geometry	Projected x- and y- coordinates, EPSG:3413	m
thick	Ice thickness	m
time	GPS measurement time since 0000-01-01	s
depthX	Depth below ice surface to reflection #X (not corrected for firn)	m

Table 5: Format of NetCDF file that contains the gridded isochrone depths and ages at normalized depths.

Variable	Description	Units
x	Projected x-coordinate, EPSG:3413	m
y	Projected y-coordinate, EPSG:3413	m
age_iso	Ages of synthetic isochrones whose depth was gridded (depth, depthstd)	ka
age	Age at normalized depth	ka
agestd	Total uncertainty in age at normalized depth	ka
depth_norm	Thickness-normalized depths whose age was gridded (age, agestd)	%
depth	Isochrone depth	m
depthstd	Total uncertainty in isochrone depth	m

7 Conclusions

We produced a second version of a dated radiostratigraphic dataset covering a substantial portion (up to 65%) of the GrIS. While far from comprehensive, as innumerable minor reflections were left untraced – let alone dated – this dataset represents an improved and potentially large-scale constraint on models of the flow of the GrIS and their sensitivity to past climate change. The inferred basic age structure of the GrIS is not significantly changed from that which M15 first described, but its development was simplified and the resulting dataset has substantially fewer tracing errors and is expected to be more robust. Finally, we modernized and further generalized the tools used to generate this radiostratigraphy – as compared to the previous version of the dataset – and expect that they could be used to either improve upon this dataset in the future for the GrIS or to accelerate Antarctic-wide mapping of radiostratigraphy.

Author contribution. JAM, MAF and AA secured funding for this study. JAM performed most of the tracing and QC, led the subsequent analysis, and drafted the manuscript. MAF aided in the analysis. JDP and JL processed the radar data. JPH traced some of the radar data. All authors reviewed and edited the manuscript.

Video supplement. Movie S1 is available at both https://doi.org/10.5281/zenodo.14531649 (MacGregor, 2024b) and also on YouTube (https://www.youtube.com/watch?v=eB0lVrQ0Awo). Because of its size (3.3 GB), it is provided separate from the dataset itself. This movie shows all 496 traced segments in chronological sequence, corrected for surface elevation as in Fig. 3e. A 50-km portion of each radargram is shown in each frame, which is translated by 20 km between each frame and is recorded at 5 frames per second. Traced and dated reflections are shown in every other frame to enable visual evaluation of the traced radiostratigraphy. An inset map of Greenland shows all traced segments, highlighting the current segment in blue and the current frame in red. The color range of the displayed radargram is rescaled for each frame to the mean ± two standard deviations of the radargram amplitudes within that frame.

Competing interests. None declared.

Acknowledgments. We thank the NASA Cryospheric Sciences program for funding this study (solicitation #NNH20ZDA001N) and the innumerable individuals who supported and performed the airborne surveys, ice-core drilling and related work that ultimately made this study possible. We thank O. Eisen, N. B. Karlsson, E. J. MacKie, T. Rieckh and D. Steinhage for valuable discussions.

References

Aschwanden, A., Fahnestock, M. A., Truffer, M., Brinkerhoff, D. J., Hock, R., Khroulev, C., Mottram, R., and Khan, S. A.: Contribution of the Greenland Ice Sheet to sea level over the next millennium, Sci. Adv., 5, eaav9396, https://doi.org/10.1126/sciadv.aav9396, 2019.

Aschwanden, A., Bartholomaus, T. C., Brinkerhoff, D. J., Truffer, M.: Brief communication: A roadmap towards credible projections of ice sheet contribution to sea level, The Cryosphere, 15, 5705–5715, https://doi.org/10.5194/tc-15-5705-2021, 2021.

Aschwanden, A. and Brinkerhoff, D. J.: Calibrated Mass Loss Predictions for the Greenland Ice Sheet, Geophys. Res. Lett., 49, https://doi.org/10.1029/2022gl099058, 2022.

Bingham, R. G., Bodart, J. A., Cavitte, M. G. P., Chung, A., Sanderson, R. J., Sutter, J. C. R., Eisen, O., Karlsson, N. B., MacGregor, J. A., Ross, N., Young, D. A., Ashmore, D. W., Born, A., Chu, W., Cui, X., Drews, R., Franke, S., Goel, V., Goodge, J. W., Henry, A. C. J., Hermant, A., Hills, B. H., Holschuh, N., Koutnik, M. R., Leysinger Vieli, G. J.-M. C., Mackie, E. J., Mantelli, E., Martín, C., Ng, F. S. L., Oraschewski, F. M., Napoleoni, F., Parrenin, F., Popov, S. V., Rieckh, T., Schlegel, R., Schroeder, D. M., Siegert, M. J., Tang, X., Teisberg, T. O., Winter, K., Yan, S., Davis, H., Dow, C. F., Fudge, T. J., Jordan, T. A., Kulessa, B., Matsuoka, K., Nyqvist, C. J., Rahnemoonfar, M., Siegfried, M. R., Singh, S., Višnjević, V., Zamora, R., and Zuhr, A.: Review Article: Antarctica's internal architecture: Towards a radiostratigraphically-informed age–depth model of the Antarctic ice sheets, EGUsphere [preprint], https://doi.org/10.5194/egusphere-2024-2593, 2024.

Bons, P. D., Jansen, D., Mundel, F., Bauer, C. C., Binder, T., Eisen, O., Jessell, M. W., Llorens, M.-G., Steinbach, F., Steinhage, D. and Weikusat, I.: Converging flow and anisotropy cause large-scale folding in Greenland's ice sheet, Nature Commun., 7, 1–6, https://doi.org/10.1038/ncomms11427, 2016.

Born, A. and Robinson, A.: Modeling the Greenland englacial stratigraphy, The Cryosphere, 15, 4539–4556, https://doi.org/10.5194/tc-2020-355, 2021.

Castelletti, D., Schroeder, D. M., Mantelli, E., and Hilger, A.: Layer optimized SAR processing and slope estimation in radar sounder data, J. Glaciol., 65, 983–988, https://doi.org/10.1017/jog.2019.72, 2019.

Cavitte, M. G. P., Young, D. A., Mulvaney, R., Ritz, C., Greenbaum, J. S., Ng, G., Kempf, S. D., Quartini, E., Muldoon, G. R., Paden, J., Frezzotti, M., Roberts, J. L., Tozer, C. R., Schroeder, D. M., and Blankenship, D. D.: A detailed radiostratigraphic data set for the central East Antarctic Plateau spanning from the Holocene to the mid-Pleistocene, Earth Syst. Sci. Data, 13, 4759–4777, https://doi.org/10.5194/essd-13-4759-2021, 2021.

Chu, W., Schroeder, D. M., Seroussi, H., Creyts, T. T., and Bell, R. E.: Complex Basal Thermal Transition Near the Onset of Petermann Glacier, Greenland, J. Geophys. Res.: Earth Surf., 123, 985–995, https://doi.org/10.1029/2017jf004561, 2018.

Cooper, M. A., Jordan, T. M., Schroeder, D. M., Siegert, M. J., Williams, C. N., and Bamber, J. L.: Subglacial roughness of the Greenland Ice Sheet: relationship with contemporary ice velocity and geology, The Cryosphere, 13, 3093–3115, https://doi.org/10.5194/tc-13-3093-2019, 2019.

Csatho, B. M., Schenk, A. F., Veen, C. J. van der, Babonis, G., Duncan, K., Rezvanbehbahani, S., Broeke, M. R. van den, Simonsen, S. B., Nagarajan, S., and Angelen, J. H. van: Laser altimetry reveals complex pattern of Greenland Ice Sheet dynamics, Proc. Natl. Acad. Sci., 111, 18478–18483, https://doi.org/10.1073/pnas.1411680112, 2014.

Culberg, R. and Schroeder, D. M.: Simulations of Englacial Radiostratigraphy from ICE Core Measurements, 2021 IEEE Int. Geosci. Remote Sens. Symp. IGARSS, 2943–2946, https://doi.org/10.1109/igarss47720.2021.9553760, 2021.

Dahl-Jensen, D., Albert, M. R, Aldahan, A., Azuma, N., Balslev-Clausen, D., Baumgartner, M., Berggren, A. M., Bigler, M., Binder, T., Blunier, T., Bourgeois, J. C., Brook, E. J., Buchardt, S. L., Buizert, C., Capron, E., Chappellaz, J., Chung, J., Clausen, H. B., Cvijanovic, I., Davies, S. M., Ditlevsen, P., Eicher, O., Fischer, H., Fisher, D. A., Fleet, L. G., Gfeller, G., Gkinis, V., Gogineni, S. P., Goto-Azuma, K., Grinsted, A., Gudlaugsdottir, H., Guillevic, M., Hansen, S. B., Hansson, M. E., Hirabayashi, M., Hong, S. M., Hur, S. D., Huybrechts, P., Hvidberg, C., Iizuka, Y., Jenk, T., Johnsen, S., Jones, T. R., Jouzel, J., Karlsson, N. B., Kawamura, K., Keegan, K., Kettner, E., Kipfstuhl, S., Kjær, H. A., Koutnik, M. R., Kuramoto, T., Köhler, P., Laepple, T., Landais, A., Langen, P. L., Larsen, L. B., Leuenberger, D., Leuenberger, M., Leuschen, C. J., Li, J., Lipenkov, V. Y., Martinerie, P., Maselli, O. J., Masson-Delmotte, V., McConnell, J. R., Millar, D. H. M., Mini, O., Miyamoto, A., Montagnat-Rentier, M., Mulvaney, R., Muscheler, R., Orsi, A J., Paden, J. D., Panton, C., Pattyn, F., Petit, J.-R., Pol, K., Popp, T. J., Possnert, G., Prié, F., Prokopiou, M., Quiquet, A., Rasmussen, S. O., Raynaud, D., Ren, J. W., Reutenauer, C., Ritz, C., Röckmann, T., Rosen, J. L., Rubino, M., Rybak, O., Samyn, D., Sapart, C. J., Schilt, A., Schmidt, A. M. Z., Schwander, J., Schüpbach, S., Seierstad, I., Severinghaus, J. P., Sheldon, S., Simonsen, S. B., Sjolte, J., Solgaard, A. M., Sowers, T. A., Sperlich, P., Steen-Larsen, H. C., Steffen, K., Steffensen, J. P., Steinhage, D., Stocker, T. F., Stowasser, C., Sturevik, A. S., Sturges, W. T., Sveinbjornsdottir, A. E., Svensson, A. M., Tison, J. L., Uetake, J., Vallelonga, P., van de Wal, R. S. W., van der Wel, G., Vaughn, B. H., Vinther, B. M., Waddington, E. D., Wegner, A., Weikusat, I., White, J., Wilhelms, F., Winstrup, M., Witrant, E., Wolff, E. W., Xiao, C. D. and Zheng, J.: Eemian interglacial reconstructed from a Greenland folded ice core, Nature, 493, 489–494, https://doi.org/10.1038/nature11789, 2013.

Das, I., Bell, R. E., Scambos, T. A., Wolovick, M., Creyts, T. T., Studinger, M., Frearson, N., Nicolas, J. P., Lenaerts, J. T. M., and Broeke, M. R. van den: Influence of persistent wind scour on the surface mass balance of Antarctica, Nat. Geosci., 6, 367–371, https://doi.org/10.1038/ngeo1766, 2013.

Delf, R., Schroeder, D. M., Curtis, A., Giannopoulos, A., and Bingham, R. G.: A comparison of automated approaches to extracting englacial-layer geometry from radar data across ice sheets, Ann. Glaciol., 61, 234–241, https://doi.org/10.1017/aog.2020.42, 2020.

Dow, C. F., Karlsson, N. B. and Werder, M. A.: Limited Impact of Subglacial Supercooling Freeze-on for Greenland Ice Sheet Stratigraphy, Geophys. Res. Lett., 45, 1481–1489, https://doi.org/10.1002/2017gl076251, 2018.

Franke, S., Bons, P. D., Westhoff, J., Weikusat, I., Binder, T., Streng, K., Steinhage, D., Helm, V., Eisen, O., Paden, J. D., Eagles, G., and Jansen, D.: Holocene ice-stream shutdown and drainage basin reconfiguration in northeast Greenland, Nat. Geosci., 15, 995–1001, https://doi.org/10.1038/s41561-022-01082-2, 2022.

Franke, S., Bons, P. D., Streng, K., Mundel, F., Binder, T., Weikusat, I., Bauer, C. C., Paden, J. D., Dörr, N., Helm, V., Steinhage, D., Eisen, O., and Jansen, D.: Three-dimensional topology dataset of folded radar stratigraphy in northern Greenland, Sci. Data, 10, 525, https://doi.org/10.1038/s41597-023-02339-0, 2023.

Franke, S., Steinhage, D., Helm, V., Zuhr, A. M., Bodart, J. A., Eisen, O., and Bons, P.: Age-depth distribution in western Dronning Maud Land, East Antarctica, from three decades of radar surveys, EGUsphere [preprint], https://doi.org/10.5194/egusphere-2024-2349, 2024.

Goelzer, H., Nowicki, S., Edwards, T., Beckley, M., Abe-Ouchi, A., Aschwanden, A., Calov, R., Gagliardini, O., Gillet-Chaulet, F., Golledge, N. R., Gregory, J., Greve, R., Humbert, A., Huybrechts, P., Kennedy, J. H., Larour, E., Lipscomb, W. H., clec'h, S. L., Lee, V., Morlighem, M., Pattyn, F., Payne, A. J., Rodehacke, C., Rückamp, M., Saito, F., Schlegel, N., Seroussi, H., Shepherd, A., Sun, S., Wal, R. van de, and Ziemen, F. A.: Design and results of the ice sheet model initialisation experiments initMIP-Greenland: an ISMIP6 intercomparison, The Cryosphere, 12, 1433–1460, https://doi.org/10.5194/tc-12-1433-2018, 2018.

Goelzer, H., Nowicki, S., Payne, A., Larour, E., Seroussi, H., Lipscomb, W. H., Gregory, J., Abe-Ouchi, A., Shepherd, A., Simon, E., Agosta, C., Alexander, P., Aschwanden, A., Barthel, A., Calov, R., Chambers, C., Choi, Y., Cuzzone, J., Dumas, C., Edwards, T., Felikson, D., Fettweis, X., Golledge, N. R., Greve, R., Humbert, A., Huybrechts, P., Le clec'h, S., Lee, V., Leguy, G., Little, C., Lowry, D. P., Morlighem, M., Nias, I., Quiquet, A., Rückamp, M., Schlegel, N.-J., Slater, D. A., Smith, R. S., Straneo, F., Tarasov, L., van de Wal, R. and van den Broeke, M.: The future sea-level contribution of the Greenland ice sheet: a multi-model ensemble study of ISMIP6, The Cryosphere, 14, 3071–3096, https://doi.org/10.5194/tc-14-3071-2020, 2020.

Hindmarsh, R. C. A., Leysinger-Vieli, G. J. -M. C., Raymond, M. J., and Gudmundsson, G. H.: Draping or overriding: The effect of horizontal stress gradients on internal layer architecture in ice sheets, J. Geophys. Res., 111, F02018, https://doi.org/10.1029/2005jf000309, 2006.

Howat, I. M., Negrete, A. and Smith, B. E.: The Greenland Ice Mapping Project (GIMP) land classification and surface elevation data sets, The Cryosphere, 8, 1509–1518, https://doi.org/10.5194/tc-8-1509-2014, 2014.

Jebeli, A., Tama, B. A., Janeja, V. P., Holschuh, N., Jensen, C., Morlighem, M., MacGregor, J. A., and Fahnestock, M. A.: TSSA: Two-Step Semi-Supervised Annotation for Radargrams on the Greenland Ice Sheet, IGARSS 2023 - 2023 IEEE Int. Geosci. Remote Sens. Symp., 00, 56–59, https://doi.org/10.1109/igarss52108.2023.10282880, 2023.

Karlsson, N. B., Dahl-Jensen, D., Gogineni, S. P., and Paden, J. D.: Tracing the depth of the Holocene ice in North Greenland from radio-echo sounding data, Ann. Glaciol., 54, 44–50, https://doi.org/10.3189/2013aog64a057, 2013.

Karlsson, N. B., Schroeder, D. M., Sørensen, L. S., Chu, W., Dall, J., Andersen, N. H., Dobson, R., Mackie, E. J., Köhn, S. J., Steinmetz, J. E., Tarzona, A. S., Teisberg, T. O., and Skou, N.: A newly digitized ice-penetrating radar data set acquired over the Greenland ice sheet in 1971–1979, Earth Syst. Sci. Data, 16, 3333–3344, https://doi.org/10.5194/essd-16-3333-2024, 2024.

Kjær, K. H., Larsen, N. K., Binder, T., Bjørk, A. A., Eisen, O., Fahnestock, M. A., Funder, S., Garde, A. A., Haack, H., Helm, V., Houmark-Nielsen, M., Kjeldsen, K. K., Khan, S. A., Machguth, H., McDonald, I., Morlighem, M., Mouginot, J., Paden, J. D., Waight, T. E., Weikusat, C., Willerslev, E. and MacGregor, J. A.: A large impact crater beneath Hiawatha Glacier in northwest Greenland, Sci. Adv., 4(11), https://doi.org/10.1126/sciadv.aar8173, 2018.

Krabill, W., Abdalati, W., Frederick, E., Manizade, S., Martin, C., Sonntag, J., Swift, R., Thomas, R., Wright, W., and Yungel, J.: Greenland Ice Sheet: High-Elevation Balance and Peripheral Thinning, Science, 289, 428–430, https://doi.org/10.1126/science.289.5478.428, 2000.

Leysinger-Vieli, G. J. M. C., Martin, C., Hindmarsh, R. C. A. and Lüthi, M. P.: Basal freeze-on generates complex ice-sheet stratigraphy, Nature Commun., 9, https://doi.org/10.1038/s41467-018-07083-3, 2018.

MacGregor, J. A., Fahnestock, M. A., Catania, G. A., Paden, J. D., Gogineni, S. P., Young, S. K., Rybarski, S. C., Mabrey, A. N., Wagman, B. M. and Morlighem, M.: Radiostratigraphy and age structure of the Greenland Ice Sheet, J. Geophys. Res. Earth Surf., 120(2), 212–241, https://doi.org/10.1002/2014jf003215, 2015a.

MacGregor, J. A., Li, J., Paden, J. D., Catania, G. A., Clow, G. D., Fahnestock, M. A., Gogineni, S. P., Grimm, R., Morlighem, M., Nandi, S., Seroussi, H. and Stillman, D. E.: Radar attenuation and temperature within the Greenland Ice Sheet, J. Geophys. Res.: Earth Surf., 120(6), 983–1008, https://doi.org/10.1002/2014jf003418, 2015b.

MacGregor, J. A., Colgan, W. T., Fahnestock, M. A., Morlighem, M., Catania, G. A., Paden, J. D., and Gogineni, S. P.: Holocene deceleration of the Greenland Ice Sheet, Science, 351, 590–593, https://doi.org/10.1126/science.aab1702, 2016a.

MacGregor, J. A., Fahnestock, M. A., Catania, G. A., Aschwanden, A., Clow, G. D., Colgan, W. T., Gogineni, S. P., Morlighem, M., Nowicki, S. M. J., Paden, J. D., Price, S. F. and Seroussi, H.: A synthesis of the basal thermal state of the Greenland Ice Sheet, J. Geophys. Res.: Earth Surf., 121(7), 1328–1350, https://doi.org/10.1002/2015jf003803, 2016b.

MacGregor, J. A., Fahnestock, M. A., Colgan, W. T., Larsen, N. K., Kjeldsen, K. K., and Welker, J. M.: The age of surface-exposed ice along the northern margin of the Greenland Ice Sheet, J. Glaciol., 66, 667–684, https://doi.org/10.1017/jog.2020.62, 2020.

MacGregor, J. A., Boisvert, L. N., Medley, B., Petty, A. A., Harbeck, J. P., Bell, R. E., Blair, J. B., Blanchard-Wrigglesworth, E., Buckley, E. M., Christoffersen, M. S., Cochran, J. R., Csathó, B. M., De Marco, E. L., Dominguez, R. T., Fahnestock, M. A., Farrell, S. L., Gogineni, S. P., Greenbaum, J. S., Hansen, C. M., Hofton, M. A., Holt, J. W., Jezek, K. C., Koenig, L. S., Kurtz, N. T., Kwok, R., Larsen, C. F., Leuschen, C. J., Locke, C.D., Manizade, S. S., Martin, S., Neumann, T. A., Nowicki, S. M. J., Paden, J. D., Richter-Menge, J. A., Rignot, E. J., Rodríguez-Morales, F., Siegfried, M. R., Smith, B. E., Sonntag, J. G., Studinger, M., Tinto, K. J., Truffer, M., Wagner, T. P., Woods, J. E., Young, D. A. and Yungel, J. K.: The scientific legacy of NASA's Operation IceBridge, Rev. Geophys., 59, https://doi.org/10.1029/2020RG000712, 2021.

MacGregor, J. A., Chu, W., Colgan, W. T., Fahnestock, M. A., Felikson, D., Karlsson, N. B., Nowicki, S. M. J., and Studinger, M.: GBaTSv2: a revised synthesis of the likely basal thermal state of the Greenland Ice Sheet, The Cryosphere, 16, 3033–3049, https://doi.org/10.5194/tc-16-3033-2022, 2022.

MacGregor, J. A., Fahnestock, M. A., Paden, J. D., Li, J., Harbeck, J. P., and Aschwanden, A.:, Dataset for: A revised and expanded deep radiostratigraphy of the Greenland Ice Sheet from airborne radar sounding surveys between 1993–2019, Zenodo, https://doi.org/10.5281/zenodo.14531734, 2024.

MacGregor, J. A.: joemacgregor/pickgui: Version 2.0.1, Submission version of PICKGUI/FENCEGUI/etc for v2 of Greenland radiostratigraphy (v2.0.1). Zenodo, https://doi.org/10.5281/zenodo.14183061, 2024a.

MacGregor, J. A.: Supplementary Video (Movie S1) for Greenland radiostratigraphy v2 dataset (Version 1). Zenodo, https://doi.org/10.5281/zenodo.14531649, 2024b.

MacKie, E. J., Field, M., Wang, L., Yin, Z., Schoedl, N., Hibbs, M., and Zhang, A.: GStatSim V1.0: a Python package for geostatistical interpolation and conditional simulation, Geosci. Model Dev., 16, 3765–3783, https://doi.org/10.5194/gmd-16-3765-2023, 2023.

Medley, B., Neumann, T. A., Zwally, H. J., Smith, B. E., and Stevens, C. M.: Simulations of firn processes over the Greenland and Antarctic ice sheets: 1980–2021, The Cryosphere, 16, 3971–4011, https://doi.org/10.5194/tc-16-3971-2022, 2022.

Mojtabavi, S., Wilhelms, F., Cook, E., Davies, S. M., Sinnl, G., Skov Jensen, M., Dahl-Jensen, D., Svensson, A., Vinther, B. M., Kipfstuhl, S., Jones, G., Karlsson, N. B., Faria, S. H., Gkinis, V., Kjær, H. A., Erhardt, T., Berben, S. M. P., Nisancioglu, K. H., Koldtoft, I., and Rasmussen, S. O.: A first chronology for the East Greenland Ice-core Project (EGRIP) over the Holocene and last glacial termination, Climate of the Past, 16, 2359–2380, https://doi.org/10.5194/cp-16-2359-2020, 2020.

Moqadam, H., and Eisen, O.: Review article: Feature tracing in radio-echo sounding products of terrestrial ice sheets and planetary bodies, The Cryosphere Discuss., https://doi.org/10.5194/egusphere-2024-1674, in review.

Moqadam, H., Steinhage, D., Wilhelm, A., and Eisen, O.: Going deeper with deep learning: automatically tracing internal reflection horizons in ice sheets, Machine Learning and Computation, https://d197for5662m48.cloudfront.net/documents/publicationstatus/229337/preprint_pdf/b283884d4a95faa94a832b33ce7e72d9.pdf, in review.

Morlighem, M., Williams, C. N., Rignot, E. J., An, L., Arndt, J. E., Bamber, J. L., Catania, G. A., Chauché, N., Dowdeswell, J. A., Dorschel, B., Fenty, I., Hogan, K., Howat, I. M., Hubbard, A. L., Jakobsson, M., Jordan, T. M., Kjeldsen, K. K., Millan, R., Mayer, L., Mouginot, J., Noël, B. P. Y., O'Cofaigh, C., Palmer, S. J., Rysgaard, S., Seroussi, H., Siegert, M. J., Slabon, P., Straneo, F., Broeke, M. R. van den, Weinrebe, W., Wood, M. and Zinglersen, K. B.: BedMachine v3: Complete Bed Topography and Ocean Bathymetry Mapping of Greenland From Multibeam Echo Sounding Combined With Mass Conservation, Geophys. Res. Lett., 44, 11,051–11,061, https://doi.org/10.1002/2017gl074954, 2017.

Morlighem, M., Williams, C. N., Rignot, E. J., An, L., Arndt, J. E., Bamber, J. L., Catania, G. A., Chauché, N., Dowdeswell, J. A., Dorschel, B., Fenty, I., Hogan, K., Howat, I. M., Hubbard, A. L., Jakobsson, M., Jordan, T. M., Kjeldsen, K. K., Millan, R., Mayer, L., Mouginot, J., Noël, B. P. Y., O'Cofaigh, C., Palmer, S. J., Rysgaard, S., Seroussi, H., Siegert, M. J., Slabon, P., Straneo, F., Broeke, M. R. van den, Weinrebe, W., Wood, M. and Zinglersen, K. B.: IceBridge BedMachine Greenland, Version 5, NASA National Snow and Ice Data Center Distributed Active Archive Center, https://doi.org/10.5067/VLJ5YXKCNGXO, 2021.

Mouginot, J., Rignot, E. J., Bjørk, A. A., Broeke, M. R. van den, Millan, R., Morlighem, M., Noel, B., Scheuchl, B., and Wood, M.: Forty-six years of Greenland Ice Sheet mass balance from 1972 to 2018, Proc. Natl. Acad. Sci., 116 (19) 9239-9244, https://doi.org/10.7280/d1mm37, 2019.

Nixdorf, U. and Göktas, F.: Spatial depth distribution of the subglacial bed and internal layers in the ice around NGRIP, Greenland, derived with airborne RES, J. Appl. Geophys., 175–182, https://doi.org/10.1016/S0926-9851(01)00062-3, 2001.

Otosaka, I. N., Shepherd, A., Ivins, E. R., Schlegel, N.-J., Amory, C., Broeke, M. R. van den, Horwath, M., Joughin, I., King, M. D., Krinner, G., Nowicki, S., Payne, A. J., Rignot, E., Scambos, T., Simon, K. M., Smith, B. E., Sørensen, L. S., Velicogna, I., Whitehouse, P. L., A, G., Agosta, C., Ahlstrøm, A. P., Blazquez, A., Colgan, W., Engdahl, M. E., Fettweis, X., Forsberg, R., Gallée, H., Gardner, A., Gilbert, L., Gourmelen, N., Groh, A., Gunter, B. C., Harig, C., Helm, V., Khan, S. A., Kittel, C., Konrad, H., Langen, P. L., Lecavalier, B. S., Liang, C.-C., Loomis, B. D., McMillan, M., Melini, D., Mernild, S. H., Mottram, R., Mouginot, J., Nilsson, J., Noël, B., Pattle, M. E., Peltier, W. R., Pie, N., Roca, M., Sasgen, I., Save, H. V., Seo, K.-W., Scheuchl, B., Schrama, E. J. O., Schröder, L., Simonsen, S. B., Slater, T., Spada, G., Sutterley, T. C., Vishwakarma, B. D., Wessem, J. M. van, Wiese, D., Wal, W. van der, and Wouters, B.: Mass balance of the Greenland and Antarctic ice sheets from 1992 to 2020, Earth Syst. Sci. Data, 15, 1597–1616, https://doi.org/10.5194/essd-15-1597-2023, 2023.

Nereson, N. A., Raymond, C. F., Waddington, E. D., and Jacobel, R. W.: Migration of the Siple Dome ice divide, West Antarctica. J. Glaciol., 44, 643–652, https://doi.org/10.3189/s002214300000214, 1998.

Parrenin, F., Hindmarsh, R. C. A., and Rémy, F.: Analytical solutions for the effect of topography, accumulation rate and lateral flow divergence on isochrone layer geometry, J. Glaciol., 52, 191–202, https://doi.org/10.3189/172756506781828728, 2006.

Panton, C.: Automated mapping of local layer slope and tracing of internal layers in radio echograms, Ann. Glaciol., 55, 71–77, https://doi.org/10.3189/2014aog67a048, 2014.

Panton, C. and Karlsson, N. B.: Automated mapping of near bed radio-echo layer disruptions in the Greenland Ice Sheet, Earth Planet. Sci. Lett., 432(C), 323–331, https://doi.org/10.1016/j.epsl.2015.10.024, 2015.

Peng, C., Zheng, L., Liang, Q., Li, T., Wu, J., and Cheng, X.: ST-SOLOv2: Tracing Depth Hoar Layers in Antarctic Ice Sheet from Airborne Radar Echograms with Deep Learning, IEEE Trans. Geosci. Remote Sens., https://doi.org/10.1109/tgrs.2024.3480698, 2024.

Rieckh, T., Born, A., Robinson, A., Law, R., and Gülle, G.: Design and performance of ELSA v2.0: an isochronal model for ice-sheet layer tracing, Geosci. Model Dev., 17, 6987–7000, https://doi.org/10.5194/gmd-17-6987-2024, 2024.

Seierstad, I. K., Abbott, P. M., Bigler, M., Blunier, T., Bourne, A. J., Brook, E., Buchardt, S. L., Buizert, C., Clausen, H. B., Cook, E., Dahl-Jensen, D., Davies, S. M., Guillevic, M., Johnsen, S. J., Pedersen, D. S., Popp, T. J., Rasmussen, S. O., Severinghaus, J. P., Svensson, A., and Vinther, B. M.: Consistently dated records from the Greenland GRIP, GISP2 and NGRIP ice cores for the past 104 ka reveal regional millennial-scale δ18O gradients with possible Heinrich event imprint, Quat. Sci. Rev., 106, 29–46, https://doi.org/10.1016/j.quascirev.2014.10.032, 2014.

Sime, L. C., Hindmarsh, R. C. A., and Corr, H.: Instruments and Methods Automated processing to derive dip angles of englacial radar reflectors in ice sheets, J. Glaciol., 57, 260–266, https://doi.org/10.3189/002214311796405870, 2011.

Sime, L. C., Karlsson, N. B., Paden, J. D., and Gogineni, S. P.: Isochronous information in a Greenland ice sheet radio echo sounding data set, Geophys. Res. Lett., 41, 1593–1599, https://doi.org/10.1002/2013gl057928, 2014.

Sullivan, C. and Kaszynski, A.: PyVista: 3D plotting and mesh analysis through a streamlined interface for the Visualization Toolkit (VTK), J. Open Source Softw., 4, 1450, https://doi.org/10.21105/joss.01450, 2019.

Winter, A., Steinhage, D., Arnold, E. J., Blankenship, D. D., Cavitte, M. G. P., Corr, H. F. J., Paden, J. D., Urbini, S., Young, D. A., and Eisen, O.: Comparison of measurements from different radio-echo sounding systems and synchronization with the ice core at Dome C, Antarctica, Cryosphere, 11, 653–668, https://doi.org/10.5194/tc-11-653-2017, 2017.

Xiong, S., Muller, J.-P., and Carretero, R. C.: A New Method for Automatically Tracing Englacial Layers from MCoRDS Data in NW Greenland, Remote Sens., 10, 43, https://doi.org/10.3390/rs10010043, 2018.